AN ABSTRACT OF THE THESIS OF

Long V. Pham for the degree of Master of Science in Electrical and Computer Engineering presented on August 11, 1995.

Title: Electrical Characterization, Maximum Charge-Maximum Voltage (Q_{max}-V_{max}) Analysis, Aging and Temperature Studies of Thiogallate Thin-Film Electroluminescent Devices.

Redacted for Privacy

Abstract approved _____
Dr. John F. Wager

Thiogallate phosphors are very attractive for use in full-color electroluminescent flat panel displays since they exhibit deep-blue light emission without the need for filtering. However, the luminance obtained from thiogallate phosphors is currently insufficient for achieving ideal full-color displays. The primary goals of this thesis are to present electrical characterization, aging, and temperature studies of blue-emitting thiogallate ($SrCaGa_2S_4$:Ce) thin-film electroluminescent (TFEL) devices, with the goal of further improving and maximizing the performance of thiogallate devices. Furthermore, a direct method for obtaining maximum charge-maximum applied voltage (Q_{max}-V_{max}) curves which is employed in the electrical characterization of TFEL devices is described.

The non-optimal performance of thiogallate devices is attributed to insufficient electron injection from the interface and an absence of band-to-band impact ionization. The electrical measurements reveal evidence for the existence of both positive and negative space charge in the thiogallate phosphor, for TFEL devices processed in various ways. The thiogallate TFEL aging mechanism is attributed to the creation of deep level, fixed charge traps at the phosphor/insulator interface. Temperature studies show evidence for thermal quenching, and two mechanisms contribute to thermal quenching in the thiogallate devices studied.

Electrical Characterization, Maximum Charge-Maximum Voltage (Q_{max}-V_{max}) Analysis, Aging and Temperature Studies of Thiogallate Thin-Film Electroluminescent Devices

by

Long V. Pham

A THESIS

submitted to

Oregon State University

in partial fulfillment of
the requirements for the
degree of

Master of Science

Completed August 11, 1995
Commencement June 1996

Master of Science thesis of Long V. Pham presented on August 11, 1995

APPROVED:

Redacted for Privacy

Major Professor, representing Electrical & Computer Engineering

Redacted for Privacy

Chair of Department of Electrical & Computer Engineering

Redacted for Privacy

Dean of Graduate School

I understand that my thesis will become part of the permanent collection of Oregon State University libraries. My signature below authorizes release of my thesis to any reader upon request.

Redacted for Privacy

Long V. Pham, Author

ACKNOWLEDGEMENTS

I would like to express my gratitude to Dr. John Wager for his guidance, advice, encouragement, and support throughout my graduate studies.

I would like to thank Planar America, especially Sey-Shing Sun, for providing samples used in this work.

In addition, I give special thanks to the EL research group, especially Paul Keir, at OSU for many useful discussions.

I also would like to thanks my parents, brothers and sisters for their support and encouragement throughout my studies. Without them this work would not have been possible.

TABLE OF CONTENTS

TABLE OF CONTENTS (Continued)

LIST OF FIGURES

LIST OF FIGURES (Continued)

Figure | Page

LIST OF FIGURES (Continued)

LIST OF FIGURES (Continued)

Electrical Characterization, Maximum Charge-Maximum Voltage (Q_{max}-V_{max}) Analysis, Aging and Temperature Studies of Thiogallate Thin- Film Electroluminescent Devices

Chapter 1 - Introduction

Electronic displays are interactive windows between humans and the artificial intelligence world of computers. The computer revolution has made interactions between humans and computers become a routine part of one's daily life. Everything from digital watches to laptop computers, from entertainment to professional applications requires an electronic display. Thus, displays are high-demand items. This information display requirement has triggered the development of portable electronic displays of minimal weight and size; these compact information displays are referred to as flat panel displays.

There are a variety of technologies under development for the production of flat panel displays. However, there are currently only three technologies that have matured to the point of high-volume commercial production: liquid crystal displays (LCD), electroluminescent (EL) displays, and plasma displays. EL technology is promising due to its simple solid-state structure and performance advantages such as high resolution, high contrast, wide viewing angle, and low weight and thickness. Its simple solid-state structure makes it insensitive to vibration, thus making EL flat panel displays attractive for military applications.

EL technology is a promising flat panel display technology. However, the commercial development of full-color EL flat panel displays is still the biggest challenge for this technology. The most difficult challenge associated with the achievement of a full-color display is the lack of an appropriate blue thin-film electroluminescent (TFEL) phosphor. Therefore, the development of an appropriate blue TFEL phosphor is the primary research objective of present day EL technology. Currently, there are two possible blue phosphor candidates: blue-green emitting strontium sulfide doped with Ce (SrS:Ce) [1] and deep-blue emitting alkaline earth thiogallates also doped with cerium ($SrCaGa_2S_4$:Ce) phosphors. [2,3] Due to the deep-blue emission without the need for filtering, the thiogallate phosphor is an attractive phosphor for use in full-color displays. For this reason, this thesis focuses on electrical characterization, aging, and temperature studies of thiogallate TFEL devices with the goal of further improving and maximizing the performance of thiogallate devices.

The remainder of the thesis is arranged as follow. Chapter 2 is a review of literature related to EL development history, fundamental device physics issues, and circuit models for TFEL devices. Chapter 3 presents electrical analysis techniques which have been employed to determine the electrical characteristics of TFEL devices. Chapter 4 presents a comparison of the electrical characteristics of thiogallate and yellow-emitting ZnS:Mn TFEL devices grown by evaporation. [4] The device physics of ZnS:Mn TFEL

devices is used as a reference point due to its almost ideal electrical characteristics and the best achieved performance to date in term of luminance and luminous efficiency. Chapter 5 presents the electrical characteristics of improved thiogallate devices, and also presents evidence of the existence of space charge generation in the phosphor and its role in determining the performance of TFEL devices. Chapter 6 presents the results of aging and temperature studies. Aging studies are undertaken to determine aging kinetics and mechanisms. Temperature studies are performed to establish the dependence of device operation on temperature and to investigate the thermal quenching mechanism of the thiogallate devices. Chapter 7 presents conclusions and suggestions for future work.

Chapter 2 - Literature Review

2.1 History and Background

Electroluminescence (EL) is a non-thermal generation of light resulting from the conversion of electrical energy into luminous energy. EL involves a very large electric field, on the order of megavolts per centimeter, which aids in the transformation of electrical energy into luminous energy.

EL was first discovered by Destriau [5] in 1936 when he observed light emission from a ZnS phosphor powder. His finding was not put into practical application until the development of SnO_2 transparent conductor in 1950. This was the beginning of the development of flat panel displays. The first single-insulator thin film electroluminescent (TFEL) structures were introduced in 1960 by Vlasenko and Popkov [6]. A double-insulating-layer structure was first reported by Russ and Kennedy [7] in 1967. These developments helped to improve the luminance and the reliability of the EL device and are the basic structures used in present day, commercial EL devices. Using the double insulator TFEL structure, Inoguchi *et al.* [8] introduced a ZnS:Mn device with a luminance of 1000 fL at a 5 kHz driving frequency in 1974 which had a lifetime of more than 10,000 hours. This result triggered the development of TFEL displays for commercial applications.

The first commercial TFEL products were introduced by Sharp [9] in 1983. Since then, Planar America and Planar International are the two additional companies that have produced TFEL displays in high volume. The first prototype full-color EL display was developed in 1993, and was available in the market in 1995. However, the development of full-color EL flat panel displays is still the biggest challenge for TFEL technology due to the lack of an appropriate blue TFEL phosphor. Therefore, one of the main goals of TFEL technology today is the development of an appropriate blue TFEL phosphor. Two possible blue phosphor candidates are the blue-green emitting SrS:Ce and the deep-blue emitting alkaline earth thiogallate ($SrCaGa_2S_4$:Ce) phosphors. Filtering is required to obtain true blue color from SrS:Ce. Therefore, thiogallate phosphors are being developed by Planar America for their flat panel displays due to their deep and pure blue emission. Recently, these phosphors were significantly improved and successfully incorporated into full-color TFEL displays by Planar America.

2.2 Sample Preparation and Basic Device Structure

The basic conventional device structure of a TFEL ZnS:Mn device is a double-insulating-layer structure shown in Fig. 2.1. These devices are fabricated on a substrate glass, Corning 7059, about 1 mm thick, using a transparent electrical conductor (i.e., indium tin oxide, ITO: In_2O_3-10 wt%

SnO_2), insulator, ZnS phosphor, insulator, metal (i.e., aluminum) structure. Atomic layer epitaxy (ALE) - deposited aluminum-titanium oxide (ATO) is used for both bottom and top insulators. The role of the insulating layers is to protect the phosphor layer from electric breakdown and to create a high electric field in the phosphor layer, in the range of 2.5-3.0 MV/cm. Thus, high dielectric constant insulating materials are desirable in the TFEL device structure.

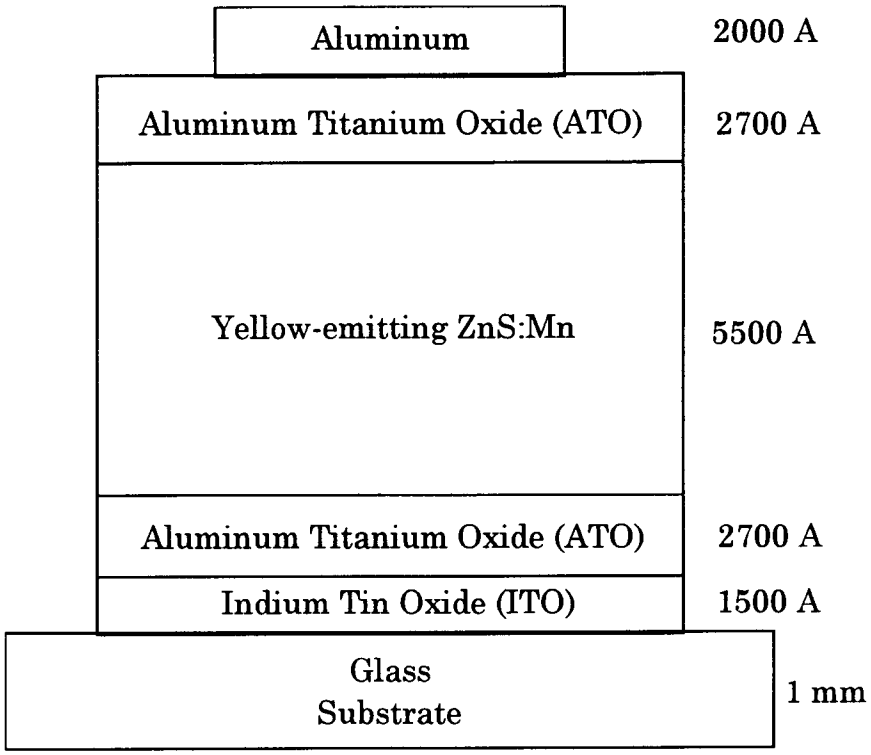

Figure 2.1. Typical yellow-emitting ZnS:Mn device structure.

2.3 TFEL Phosphors

The TFEL phosphor consists of a host material and light-emitting centers, commonly called luminescent centers or impurity centers. A good host material must have a bandgap in the range of approximately 3.5 to 4.5 eV, a low dielectric constant, good crystallinity, high breakdown field (of order, or greater than, 1.5 MV/cm), and be able to withstand high temperature processing. A large band gap ensures that the ground and excited states of luminescent centers occur within the band gap. A low dielectric constant ensures that most of the applied voltage drops across the phosphor layer. Good crystallinity allows electrons to accelerate efficiently inside the phosphor without losing kinetic energy to the lattice via scattering. High breakdown field ensures that the onset of electron emission occurs at a sufficiently high field so that electrons gain sufficient kinetic energy to efficiently impact excite the luminescent centers.

Most phosphor hosts belong to the II-VI compound group. The three most common TFEL phosphors are: ZnS (E_g = 3.6 eV), alkaline-earth sulfides CaS (4.4 eV) and SrS (4.3 eV), and alkaline-earth thiogallates (4.2-4.4 eV). To achieve a desired emitting color, a host material is doped with selected luminescent impurities. Besides Mn, all other common dopant luminescent impurities are rare-earth elements. Until now, the yellow-emitting ZnS:Mn phosphor is the TFEL phosphor with the best performance in terms of luminance and luminous efficiency. [10] For this reason, the device physics and

operation of ZnS:Mn TFEL devices is used as a reference point for comparing the performance of the optical and electrical characteristics of many other TFEL phosphors.

Red, green, and blue are the primary colors required for multicolor display applications. Red can be obtained by filtering the broad emission spectrum of the yellow-emitting ZnS:Mn phosphor, [11] which ranges from green to red with a peak at 585 nm. ZnS:Tb is a suitable green EL. The chromaticity of red-filtered ZnS:Mn and ZnS:Tb [12,13] phosphors are close to that used in standard CRT color displays. The most promising blue phosphors are the green-blue emitting SrS:Ce and the deep blue emitting alkaline-earth thiogallate phosphors, MGa_2S_4 (M: Ca, Sr or Ba), activated by cerium, Ce^{3+}. The deep-blue emission without the need for filtering makes thiogallate phosphors very attractive for use in multicolor displays. However, the luminance obtained from blue thiogallate phosphors is currently insufficient for achieving the desired 3:6:1 red-green-blue luminescent ratio required for an ideal full-color display.

The thiogallate phosphor consists of a MGa_2S_4 (where M may be Ca, Sr or Ba) host material and cerium (Ce) blue emitting centers, The optimum doping concentration of Ce in the phosphor is typically 6 percent by weight. Increasing the concentration above this critical value causes a reduction of luminescence in the device due to concentration quenching. Concentration quenching involves an interaction between the excited cerium

centers which increases the probability of non-radiative decay within the phosphor.

2.4 Device operation

The EL device operates [14,15,16] by applying a large, external ac voltage across the aluminum and ITO electrodes. A typical test waveform for characterizing EL devices is a 1 kHz symmetric waveform of bipolar pulses, as shown in Fig. 2.2, with 5 μs rise and fall times and a pulse width of 30 μs.

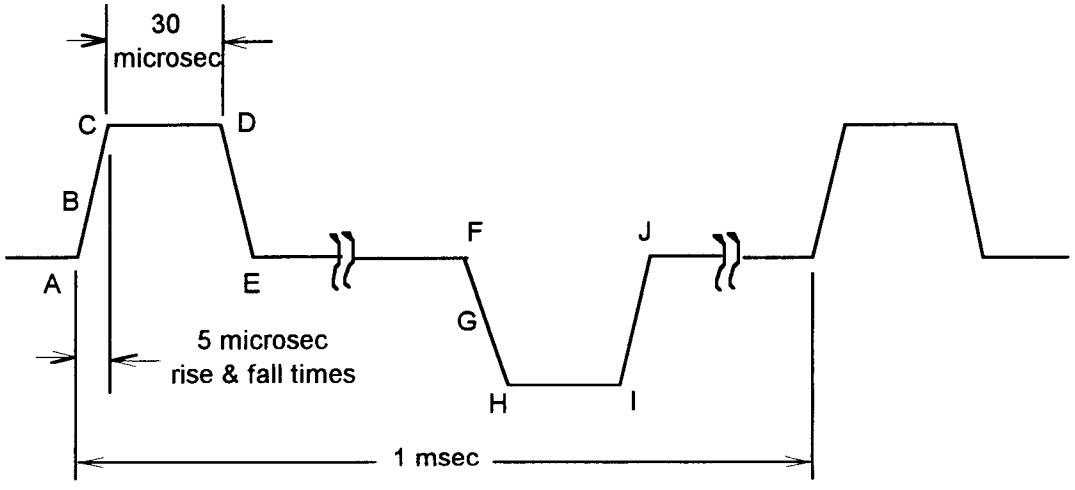

Figure 2.2. Standard bipolar pulse driving waveform.

When an ac voltage is applied across the external electrodes, a portion of the applied voltage drops across the insulating layers and the rest appears across the phosphor layer, giving rise to the phosphor electric field. Ideally,

it is desirable to have most of the applied voltage drop across the phosphor layer. The phosphor field increases with increasing external applied bias until a phosphor electric field on the order of 1.5-2.5 MV/cm is reached. When a critical field is reached, the phosphor layer breaks down and gives rise to conduction in the phosphor layer through tunnel emission of interface electrons from the cathode insulator/phosphor interface into the conduction band of the phosphor layer (see Fig. 2.3). Once emitted into the conduction

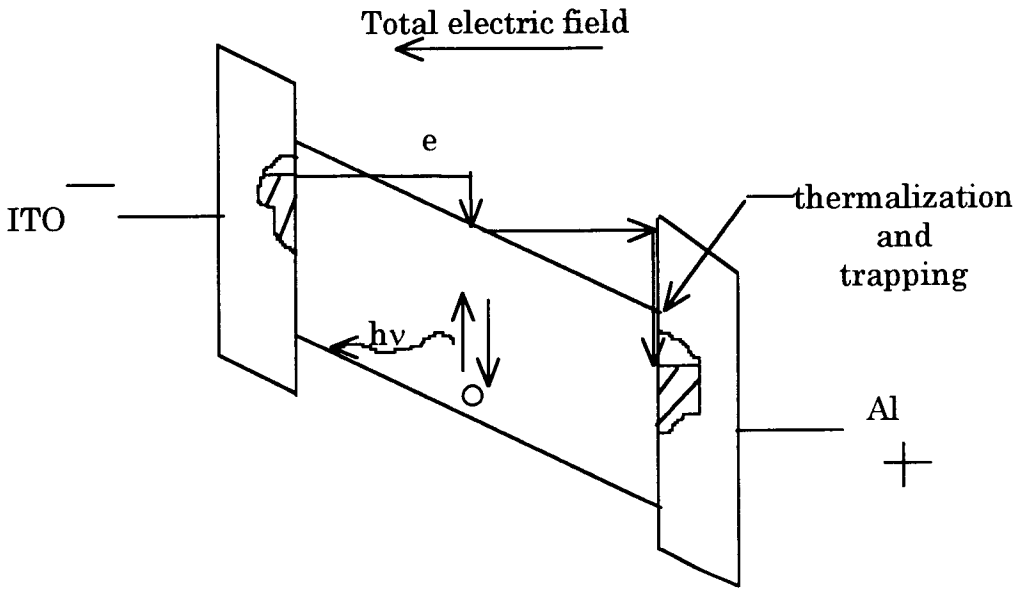

Figure 2.3. EL device under bias.

band of the phosphor layer, electrons are accelerated, gain kinetic energy from the high electric field, and travel across the phosphor layer. After gaining sufficient kinetic energy, these high energy electrons are commonly called hot electrons. Some of these hot electrons collide with luminescent

centers and excite them into higher energy excited states. When these excited impurity atoms relax or decay back to their ground states, they give off their excess energy in the form of light. After colliding with the impurity centers, the hot electrons continue to gain kinetic energy from the electric field until they reach the anode interface. Upon reaching the anode interface, the hot electrons dissipate their kinetic energy to the lattice in a process known as thermalization. Subsequently, these thermalized electrons are trapped in deep states at the anode interface.

A better understanding of the physics of EL device operation may be obtained via simplified energy band diagrams. Figure 2.4 shows an energy band diagram of an EL device in equilibrium in an idealized, flat- band

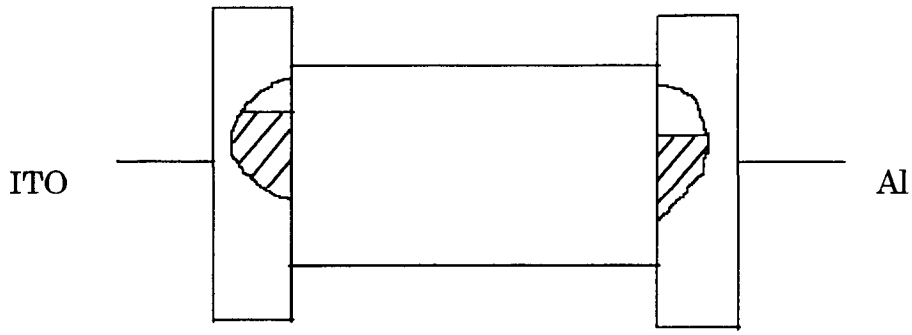

Figure 2.4. Energy band diagram at zero bias, assuming a flat-band condition.

condition. From this figure, note that the device is not necessarily symmetrical, even when the same insulating material and thickness is used

for both of the insulators. Differences may arise during processing, giving rise to differences in the interface state densities and distributions at the two interfaces.

Assuming that aluminum and ITO are both perfect conductors, when a positive voltage is applied to a virgin device, the applied voltage drops across the two insulating layers and the phosphor. Due to the initial flat-band condition of the device, the internal phosphor field is totally set up by the applied voltage and the phosphor field increases with increasing applied voltage until tunnel emission occurs. The applied voltage at the onset of

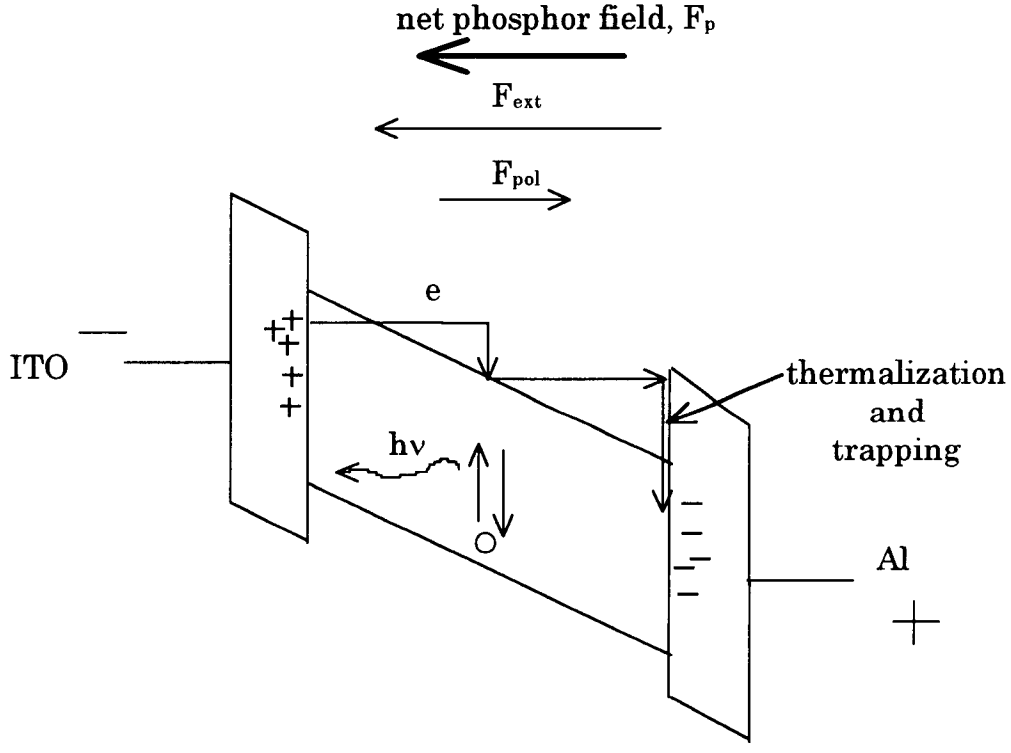

Figure 2.5. EL device during a positive bias voltage greater than the threshold voltage.

electron emission, without the presence of polarization charge (which is discussed subsequently), is defined as the threshold voltage of the device. As the applied voltage is further increased above the threshold voltage, as shown in Fig. 2.5, internal electron conduction occurs across the phosphor layer and the phosphor field may be effectively clamped if there is sufficient electron tunnel-emission from interface states. This so-called field-clamping is a consequence of the build-up of a polarization field which opposes the applied electric field, F_{ext}. This opposing polarization field arises from

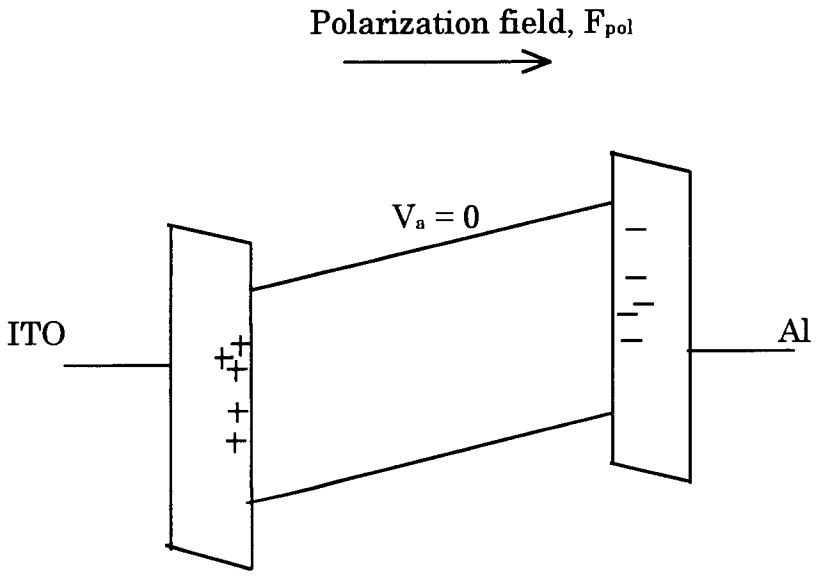

Figure 2.6. EL device at zero bias after the application of a positive voltage pulse.

positive charge left behind by the emission of electrons from the cathode interface and negative charge accumulation at the anode interface. The

phosphor field, which is effectively clamped and constant during the rising portion of the applied voltage above threshold, is called the steady-state field, F_{ss}. Once the applied voltage returns to zero, the phosphor field remains non-zero but changes polarity, as shown in Fig. 2.6, due to the polarization electric field set up by the previous electron conduction process. The phosphor field at zero bias is called the polarization field, F_{pol}, and the charge at the interfaces is called the polarization charge, Q_{pol}. Depending on the trap interface depths and the magnitude of the polarization field, some of this polarization charge can tunnel-emit from shallow interface states during the zero bias portion of the waveform. The total charge emitted during the zero bias portion of the waveform is called the leakage charge, Q_{leak}.

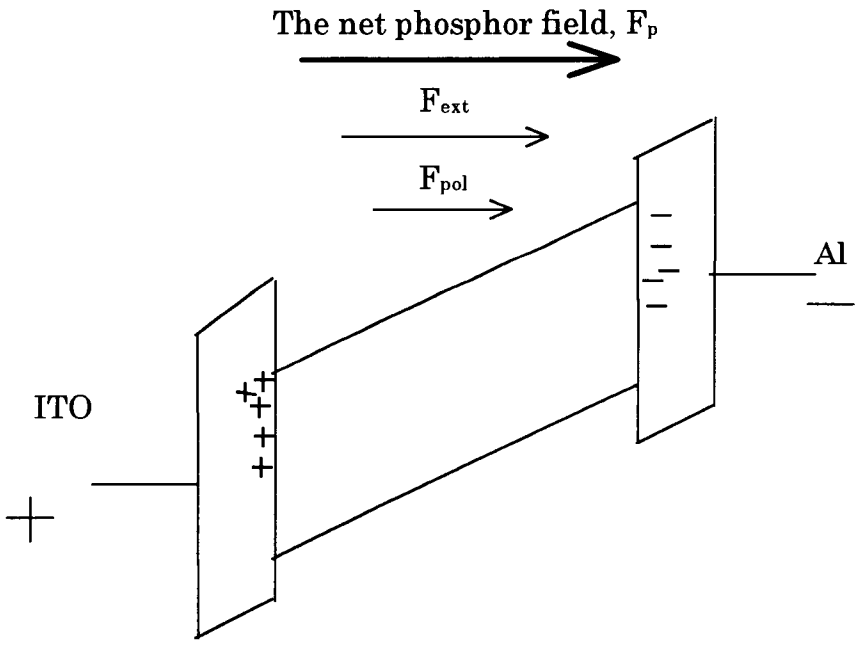

Figure 2.7. EL device at the onset of conduction in the presence of polarization charge from a previously applied negative voltage pulse.

Figure 2.7 illustrates an energy band diagram for the subsequent, negative bias pulse. Note that during this voltage pulse the polarization charge, or polarization field, assists the external electric field in the emission of electrons from interface trap states so that the threshold voltage of this pulse is less than that of the previous pulse in which there was no polarization charge. The voltage required for the onset of internal conduction in the presence of polarization charge is called the turn-on voltage. This result indicates that the leakage charge, mentioned previously, has a negative effect in the device operation since it reduces the number of

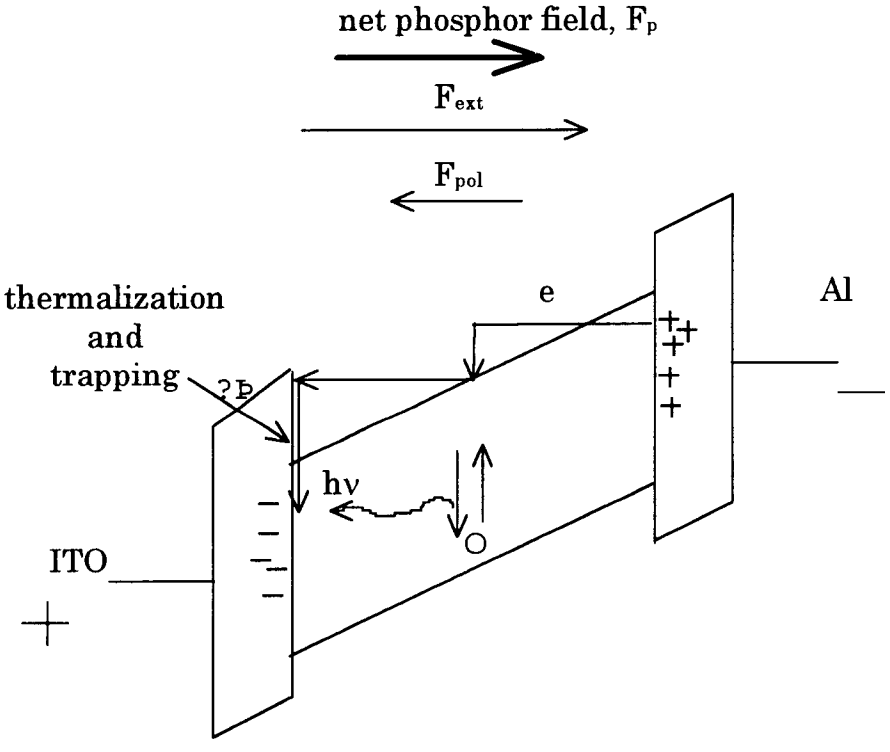

Figure 2.8. EL device during negative bias.

electrons available for transfer during the high electric field and also increases the turn-on voltage. Polarization charge build-up is desirable since it aids in reducing the amount of applied voltage required for conduction. Figure 2.8 shows the EL device after the onset of conduction upon application of a negative bias.

2.5 The SPICE Circuit Model

Figure 2.9 shows the simplest equivalent circuit model [16,17] for SPICE simulation of an electroluminescent device. It consists of two insulator capacitors, C_{i1} and C_{i2}, connected in series with the phosphor capacitance, C_p, which is in parallel with a pair of Zener diodes. The breakdown voltage of

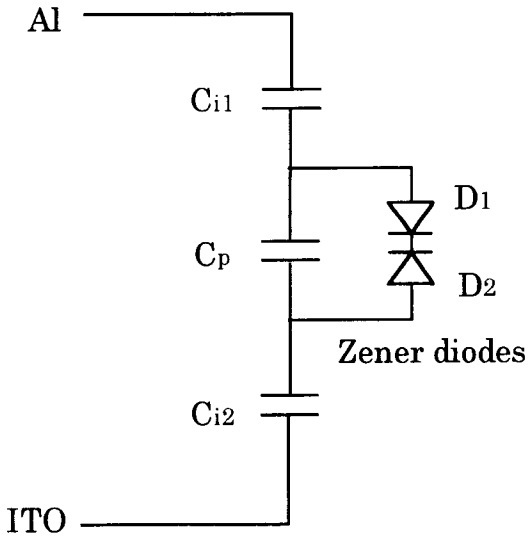

Figure 2.9. Simplest circuit model of an EL device.

these Zener diodes is set to the threshold voltage of the EL device at which the onset of tunnel emission or electron conduction occurs in the phosphor layer. Under ideal device operation, when there is sufficient electron emission from the interface, the Zener diodes effectively shunt the phosphor capacitor due to electron conduction through the phosphor after breakdown. When breakdown occurs, the capacitance seen looking into the EL device is exclusively equal to the total insulator capacitance. This circuit models an ideal EL device; it is insufficient to model an actual EL device under real device operation and to explain the detailed experimental characteristics of EL devices.

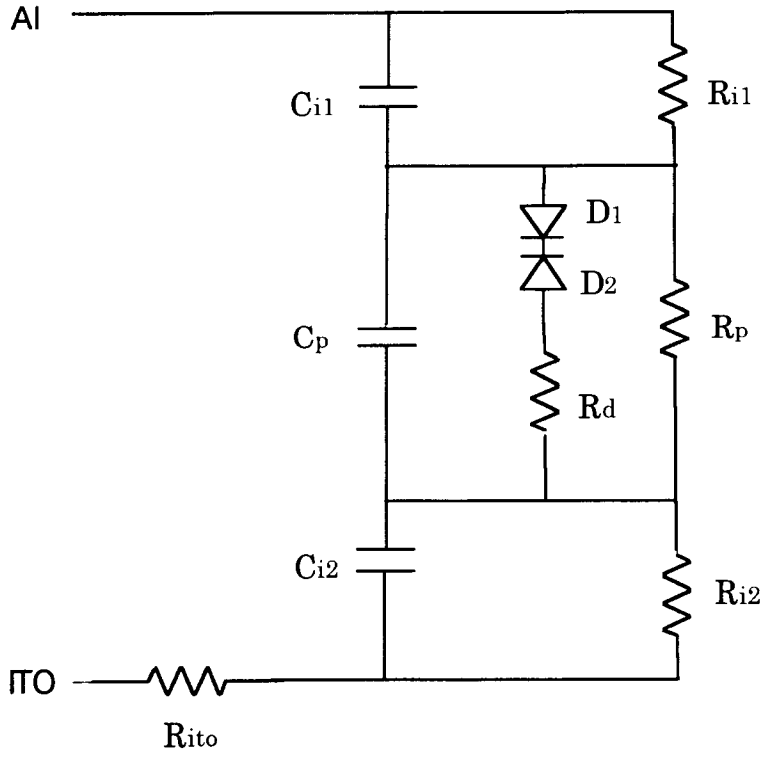

Figure 2.10. Davidson's EL device circuit model.

Davidson *et al.* [18] developed an improved equivalent circuit model and performed SPICE simulation using this improved model. Davidson et al. modified the previous model with the addition of five resistors to account for dc leakage and current limiting in the phosphor layer. Their modified circuit model is shown in Fig. 2.10. In this model, R_{ito} represents the resistance of the ITO layer (typically, the sheet resistance of ITO thin films is in a range of 5 to 10 ohms per square). R_{i1}, R_{i2}, and R_p represent the resistance of the insulator layers and phosphor layer, respectively. R_d connected in series

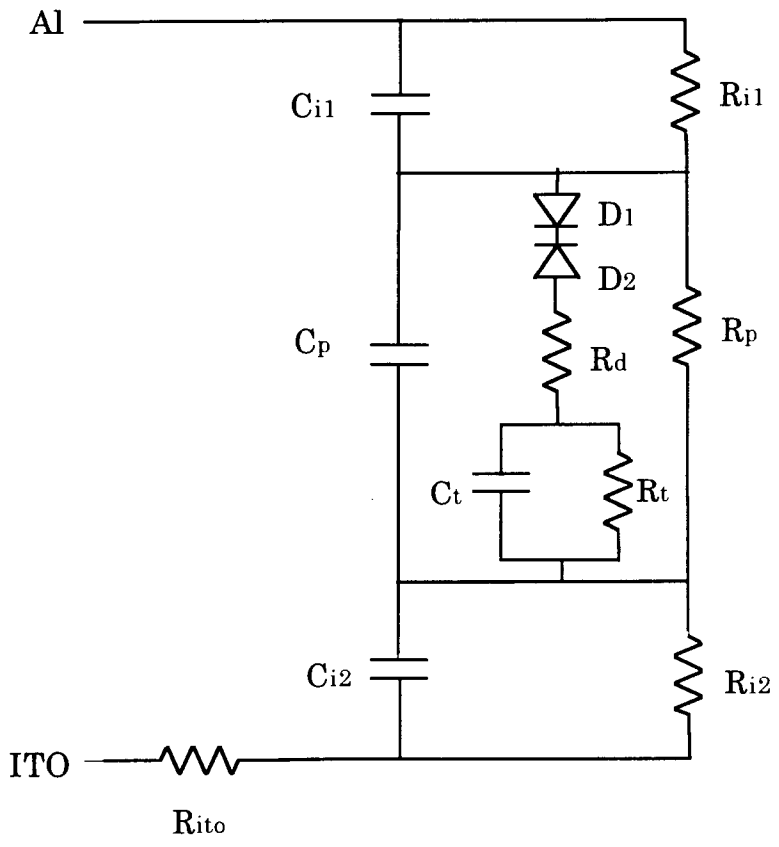

Figure 2.11. Douglas's EL device circuit model.

with the diodes is used to model the limitation of current flow during conduction in the phosphor layer. This modified circuit model was deduced in order to explain experimental results obtained from C-V analysis. R_d is responsible for the C-V slope during the portion of the waveform in which conduction across the phosphor occurs.

However, the modified equivalent circuit of Davidson *et. al.* was insufficient for modeling the waveform dependence of the turn-on voltage and the relaxation charge that accounts for the decrease of the phosphor field during the constant and maximum portion of the applied voltage waveform. Douglas [19] refined the circuit model further by adding two more parallel elements in series with the Zener diodes and the resistance R_d, as shown in Fig. 2.11, to account for the relaxation charge that causes a decrease in the phosphor field.

Douglas's circuit model provides a fairly good description of the electrical characteristics of a well-behaved EL device, assuming that no space charge generation occurs inside the phosphor. However, experimental results obtained recently reveal that space charge generation plays an important role in the operation of several types of EL devices. Therefore, a circuit model that accounts for space charge generation is needed.

Chapter 3 - Electrical Analysis Techniques

3.1 Introduction

This chapter presents the electrical measurement techniques that have been employed to determine the electrical characterization of EL devices. The techniques commonly used to electrically characterize EL devices are capacitance-voltage (C-V) [20], internal charge-phosphor field (Q-F_p) [21], external charge-voltage (Q-V), [17,22] and maximum charge-maximum applied voltage (Q_{max}-V_{max}). [23,24] From the C-V and Q-V techniques the device capacitance of the EL stack before and after breakdown can be obtained. Also, the total capacitance of the EL device can be accurately determined from these two techniques. However, determination of the insulator capacitance is not always simple; it is easily assessed if field-clamping occurs, but this is often not the case. The Q-F_p technique provides information about internal device operation which depends strongly on the internal conduction charge and the phosphor field. The Q_{max}-V_{max} method originates from the Q-F_p technique and provides information related to electron emission and capture processes and charge multiplication or impact ionization in the bulk region.

3.2 Experimental Setup and Waveform

The basic circuit used to accomplish the electrical characterization of a

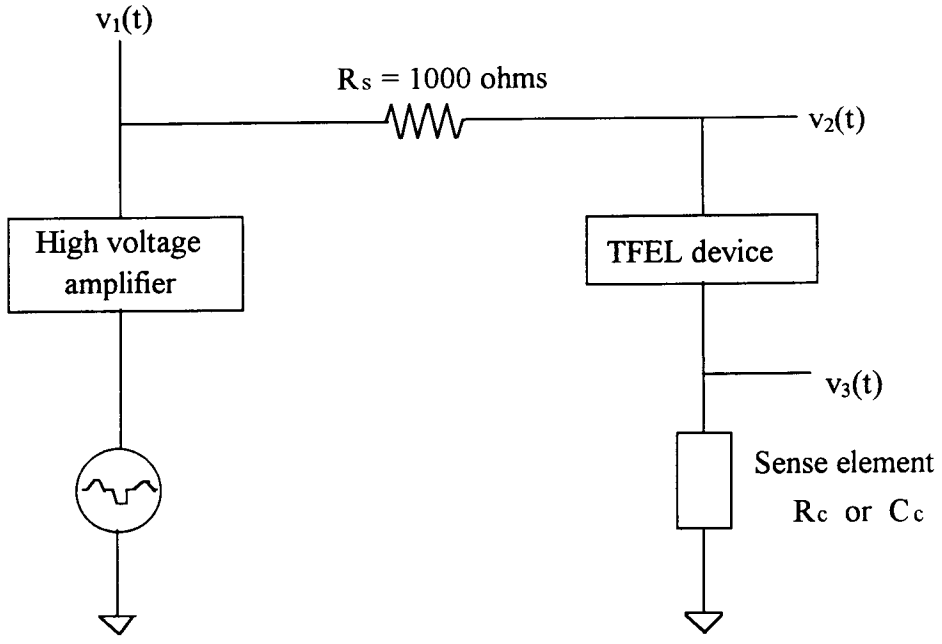

Figure 3.1. Basic circuit for TFEL electrical characterization.

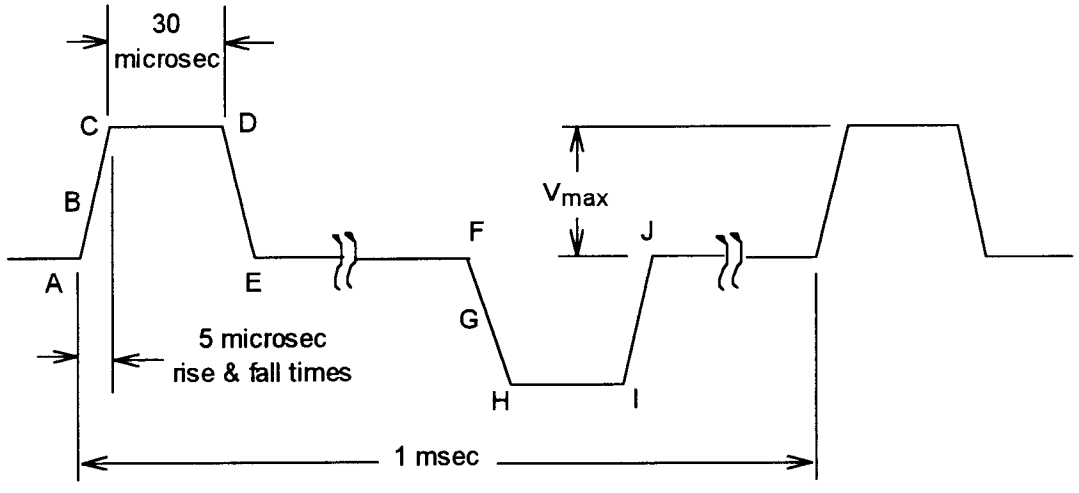

Figure 3.2. Standard symmetric bipolar pulse waveform used for EL electrical characterization.

TFEL device is shown in Fig. 3.1. It consists of an arbitrary waveform generator (Wavetek model 395) which provides a 1 kHz symmetric waveform of bipolar pulses, a high voltage gain amplifier using Apex model PA-95 operational amplifiers, a series resistor (R_s = 1000 ohms), the TFEL device, and a sense element. A resistor is used as the sense element (i.e., R_c = 10 ohms) for C-V measurement while a sense capacitor (C_c = 110.8 nF) is used for Q-V, Q-F_p, and Q_{max}-V_{max} measurements. The symmetric bipolar pulse waveform is shown in Fig. 3.2; the labels A-J are used to denote certain critical points in the waveform, as discussed in later sections of this chapter. The voltages labeled $v_1(t)$, $v_2(t)$, and $v_3(t)$ are monitored using a Tektronix model TDS 420 digitizing oscilloscope.

3.3 Capacitance-Voltage (C-V) Analysis

C-V analysis is accomplished using a small resistor, R_c = 10 ohms, as a current sense resistor. The C-V curve is obtained by plotting the dynamic capacitance, $C(v_2 - v_3)$, as a function of the voltage across the TFEL device, $v_{el}(t)$, given by

$$C(t) = \frac{i(t)}{\frac{d[v_2(t) - v_3(t)]}{dt}} \qquad (3.1)$$

where the current is obtained from the current across the sense resistor,

$$i(t) = \frac{v_3(t)}{R_c} \; . \qquad (3.2)$$

A typical C-V curve for an evaporated ZnS:Mn TFEL device is shown in Fig. 3.3 which demonstrates ideal device operation. C_t is the total capacitance of the TFEL stack measured prior to the initiation of conduction within the phosphor. C_i is the total capacitance of the two insulators which sandwich the phosphor. This measured capacitance is only equal to the insulator capacitance if the extent of conduction within the phosphor is sufficient to completely shunt the phosphor capacitance and if there is no build up of space charge within the phosphor. V_{to1}, V_{to2}, and V_{to3} respectively denote the external applied voltage at which conduction is initiated, the applied voltage corresponding to turn-on as measured from a charge-voltage (Q-V) curve, and the applied voltage at which field-clamping occurs (if indeed it does occur). The capacitance rise beginning at about 190 V in Fig. 3.3 arises from Eqn. (3.1) because the current decays more rapidly than the derivative of the voltage across the TFEL device. [18] This feature is ignored when interpreting a C-V curve. Finally, note that the slope of the C-V curve is related to the pre-clamping density of interface states [18] as follows:

$$Q_{ss} = \frac{C_i^2}{2qA}\frac{C_t}{C_p}\left[\frac{\Delta C}{\Delta V}\right]^{-1} \qquad (3.3)$$

where C_p is the phosphor capacitance and A is the TFEL device area. It is evident from Eq. 3.3 that a C-V curve with a shallow slope is indicative of a large density of pre-clamping interface states compared to when a C-V curve

has a steep slope with an abrupt transition between V_{to1} and V_{to3}.

The C-V curve shown in Fig. 3.3 represents the C-V characteristics of an ideal TFEL ZnS:Mn device. However, the experimental results from other

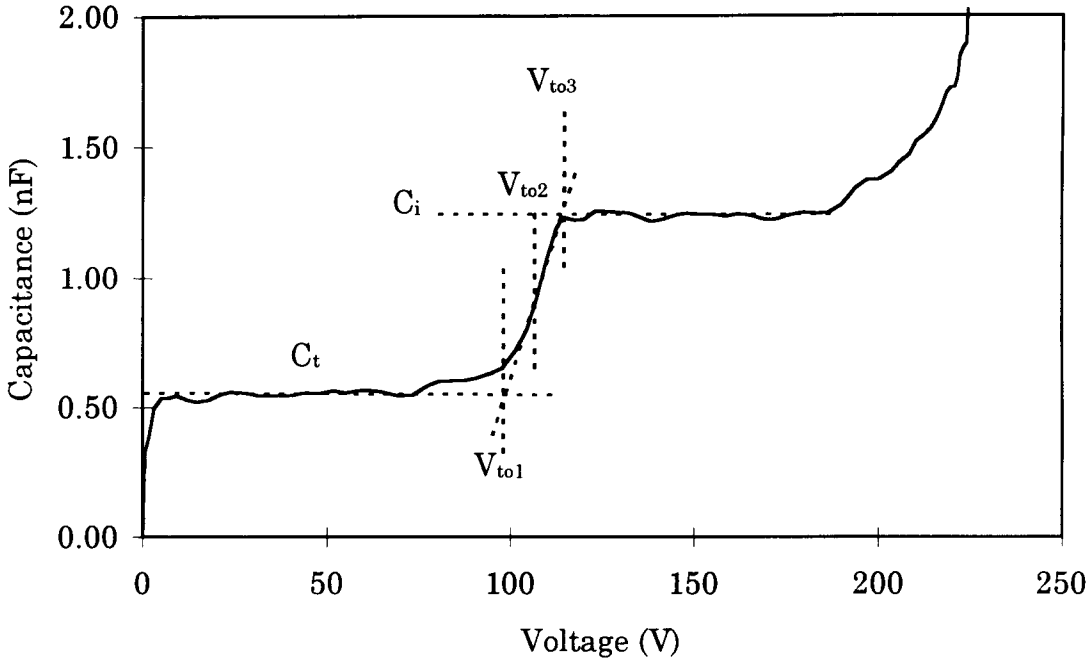

Figure 3.3. Typical C-V plot of a ZnS:Mn EL device.

devices (e.g. thiogallate and SrS:Ce) show non-ideal behavior of the C-V curve. The measured capacitance can be greater or less than the physical capacitance. Therefore, to better understand the C-V curve some additional information is needed, as shown in Fig. 3.4. In Fig. 3.4, C_i is the total physical insulator capacitance, which is calculated from known thicknesses and the dielectric constants of the two insulators which sandwich the

phosphor. C_{eff} is the measured, effective insulator capacitance of the device. As a measure of the performance of the EL device, a ratio of C_{eff} to C_i is used. Let M to be the ratio of C_{eff} to C_i:

$$M = \frac{C_{eff}}{C_i} \quad . \tag{3.4}$$

The charge sourcing performance of an EL device is assessed according to its value of M, as given below:

M = 1: Sufficient charge emission from the interface to exactly balance the ramping rate of the external voltage ($C_{eff} = C_i$).

M < 1: Insufficient charge emission from the interface ($C_{eff} < C_i$).

M > 1: Space charge creation in the phosphor layer by charge multiplication ($C_{eff} > C_i$).

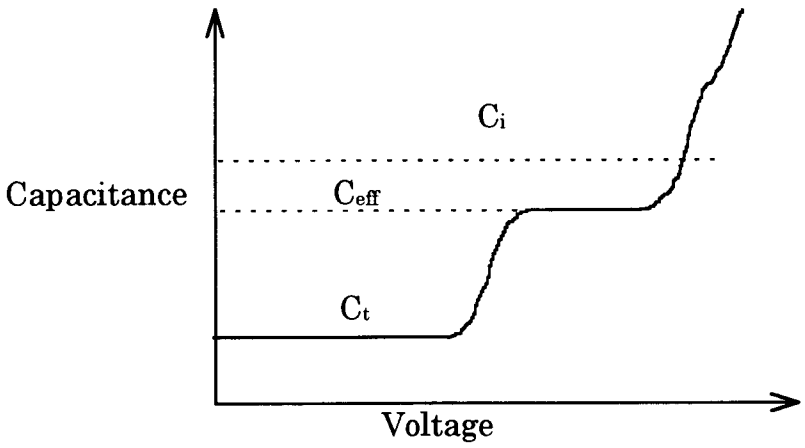

Figure 3.4. Typical C-V plot of a non-ideal EL device.

3.4 Internal Charge-Phosphor Field (Q-F_p) Analysis

Q-F_p analysis is accomplished using C_c = 110.8 nF as the sense element shown in Fig. 3.1. As derived from electrostatics, the instantaneous charge in the phosphor is given by [25]

$$q_{\text{int}}(t) = \frac{C_i + C_p}{C_i} C_c v_3(t) - C_p[v_2(t) - v_3(t)]. \tag{3.5}$$

and the instantaneous average electric field in the phosphor is given by

$$f_p(t) = \frac{1}{d_p}\left\{\frac{C_c v_3(t)}{C_i} - [v_2(t) - v_3(t)]\right\} \tag{3.6}$$

where d_p is the phosphor thickness. A Q-F_p curve is obtained by plotting $q_{int}(t)$ versus $f_p(t)$, as assessed from Eqns. (3.5) and (3.6), respectively. A typical Q-F_p curve for an evaporated ZnS:Mn TFEL device is shown in Fig. 3.5. The labels A-J correspond to the critical points of the applied voltage waveform, as indicated in Fig. 3.2.

A brief discussion of features of the Q-F_p curve shown in Fig. 3.5 is now provided to facilitate the later use of these curves. The curve labeled A in Fig. 3.5 corresponds to the onset of the positive voltage pulse to the Al electrode. Note that Q and F_p are nonzero at point A; this is due to the existence of polarization charge stored at the phosphor/insulator interface set up by the previous pulse of opposite polarity. The polarization charge associated with point A is denoted Q^-_{pol} where the negative superscript denotes that this charge arises from the negative pulse. The BC portion of

Fig. 3.5, where F_p is constant, corresponds to the portion of the voltage waveform above threshold and during the rising portion of the applied voltage pulse. BC defines the steady-state field, F_{ss}, in which the rate of increase of the phosphor field due to the external bias slew rate is equal to the decrease in the rate of the

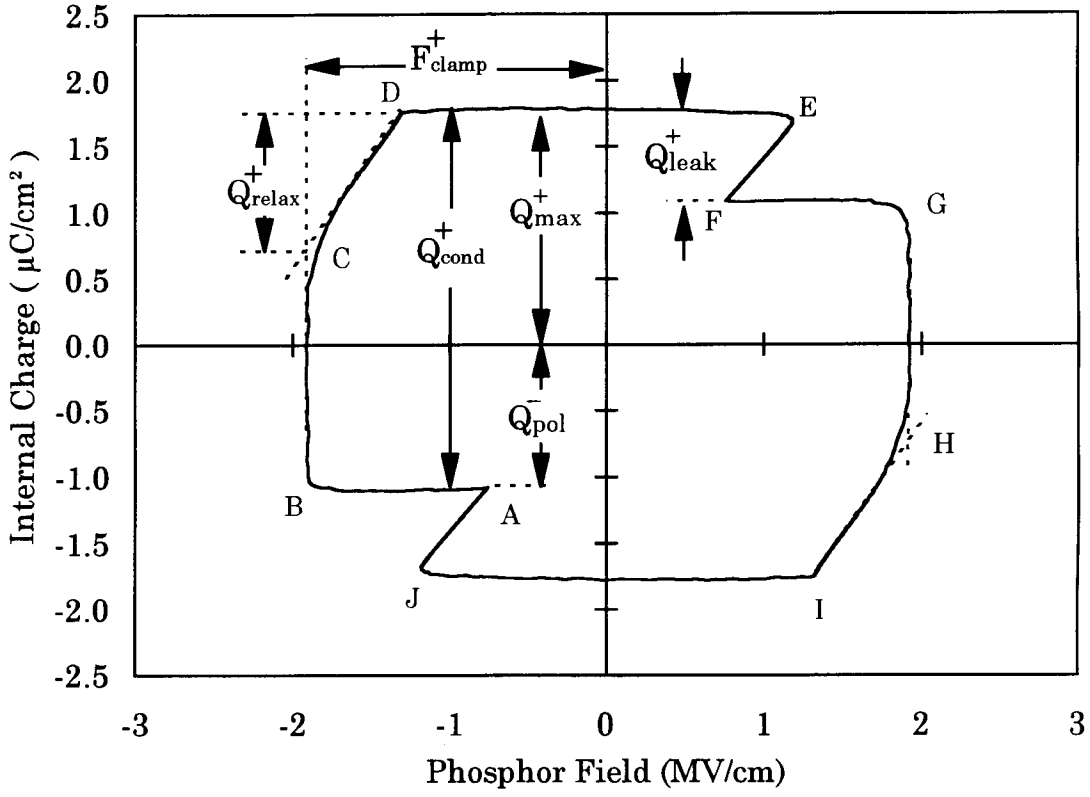

Figure 3.5. Typical Q-F_p plot for a ZnS:Mn EL device.

phosphor field due to the transport of electrons across the phosphor and the concomitant reduction of the polarization field. The steady-state field, F_{ss}, may be designated as the clamping field if F_{ss} is independent of the

maximum applied bias, V_{max}, for Vmax's above threshold. As demonstrated in the following chapter, field-clamping is not always observed in TFEL devices. Portion CD of Fig. 3.5 is due to relaxation of the phosphor field [19] as more charge is transported across the phosphor during the portion of the applied voltage pulse in which the waveform is constant at its maximum value. The charge transported during this portion of the waveform is denoted relaxation charge, Q_{relax}. As indicated in Fig. 3.5, Q^{+}_{cond} is the conduction charge transported during the positive voltage pulse. The DE portion of the Q-F_p curve occurs during the falling edge of the applied voltage waveform. The polarity of the phosphor field reverses during the DE portion of the waveform because the external bias is removed and the remaining field is due to the transported charge which is subsequently trapped and sets up a polarization field. Portion EF of the Q-F_p curve occurs during the portion of the waveform in which no external voltage is applied. Leakage charge, Q^{+}_{leak}, is assessed during the EF portion of the waveform due to the emission of shallow interface states due to the existence of the polarization field in the phosphor. The remainder of the Q-F_p curve from F to A is similar to the A to F portion of the curve just described except that the external applied voltage pulse is of opposite polarity. It is important to note that all of the charges labeled in the Q-F_p plot are internal charges and, thus, the magnitude of these charges may be directly compared. This is an important advantage of Q-F_p compared to Q-V analysis.

The Q-F_p plot shown in Fig. 3.5 is typical for an evaporated TFEL ZnS:Mn device, which has an almost ideal behavior. However, other devices, such as thiogallate and SrS:Ce devices exhibit non-ideal characteristics. Figure 3.6 shows how the Q-F_p curve would vary for different values of M.

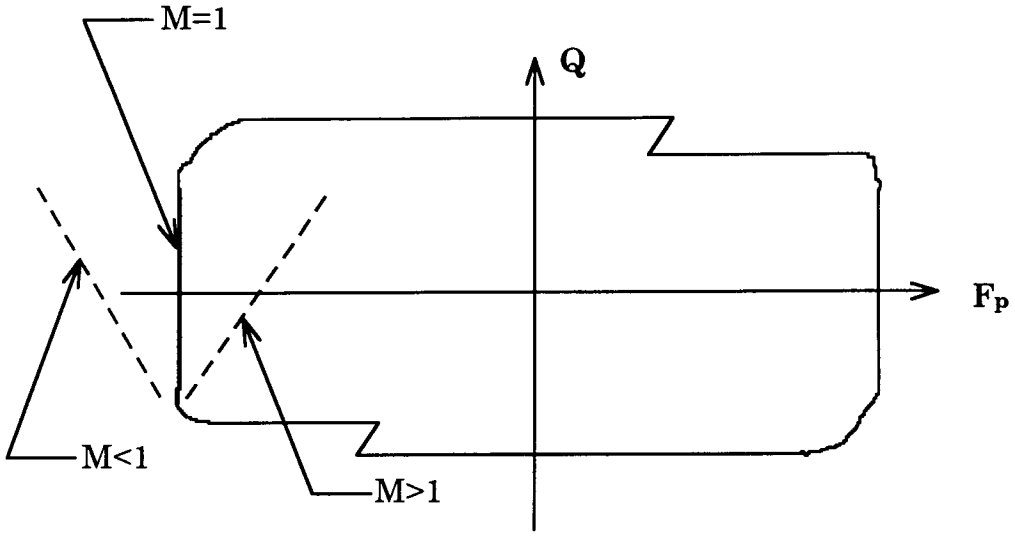

Figure 3.6. General variation of a Q-F_p plot for an EL device.

3.5 External Charge-Voltage (Q-V) Analysis

Q-V analysis is accomplished using C_C = 110.8 nF as the sense element shown in Fig. 3.1. The instantaneous external charge, $q_{ext}(t)$, is given by

$$q_{ext}(t) = C_c v_3(t) \qquad (3.7)$$

A Q-V curve is generated by plotting $q_{ext}(t)$ versus the applied voltage across EL device, $v_{el}(t)$. A typical Q-V curve for an evaporated ZnS:Mn TFEL device is shown in Fig. 3.7. Features of the Q-V curve are similar to that of the Q-F_p

curve, therefore the same discussion as presented for Q-F_p analysis could be used to describe the Q-V curve. However, it is important to note that all of the charges labeled in the Q-F_p plot are internal charges, whereas the charges labeled on the Q-V are external charges. Note that internal and external charges are the same for conduction and relaxation charges, but are not the same for polarization and leakage charges [22]. External charge and internal polarization and leakage charges are related by a capacitive ratio; for example,

$$Q_{pol}(external) = \frac{C_i}{C_i + C_p} Q_{pol}(internal). \qquad (3.8)$$

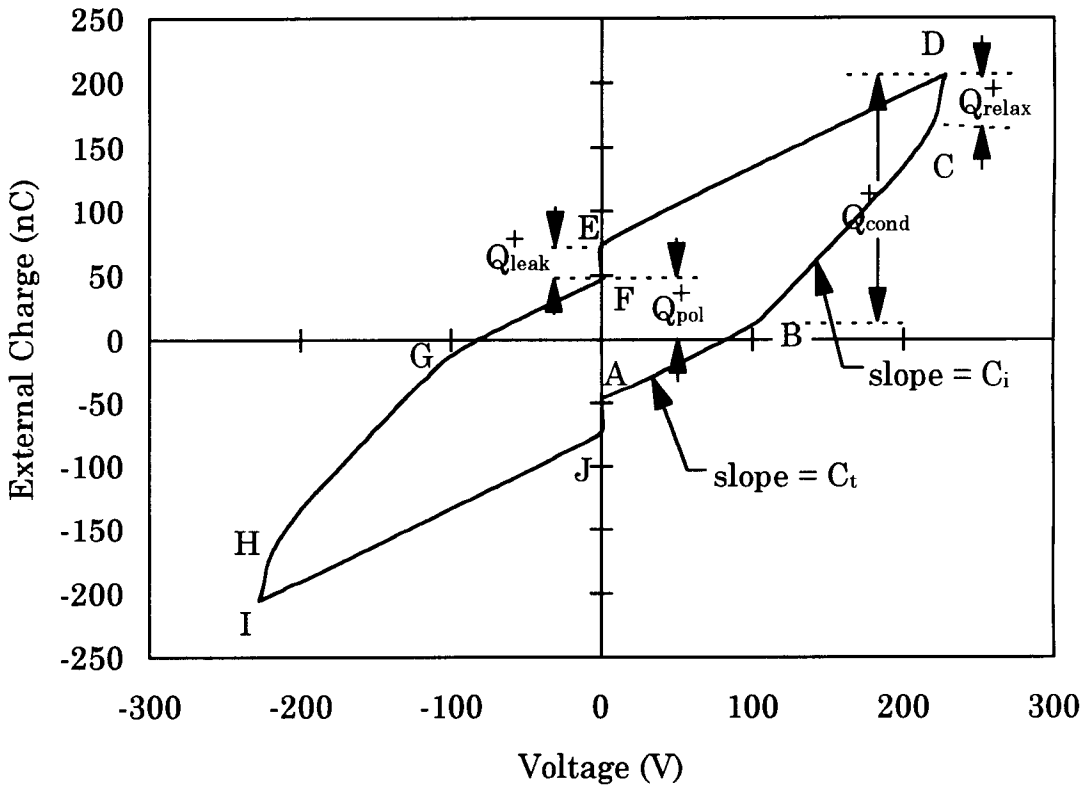

Figure 3.7. Typical Q-V plot of a ZnS:Mn EL device.

Note that the C_t and C_i obtained from C-V analysis can also be obtained from Q-V analysis by observing the slope of the Q-V curve in regions AB and BC, respectively, for the positive applied voltage, and regions FG and GH, respectively, for the negative bias voltage.

3.6 Maximum Charge-Maximum Voltage (Q_{max}-V_{max}) Analysis

Q_{max} is defined in the Q-F_p curve shown in Fig. 3.5. It is the net charge accumulated at the interface with respect to the flat band condition or charge neutral condition, as shown in Fig. 2.4, after a voltage pulse. A Q_{max}-V_{max}

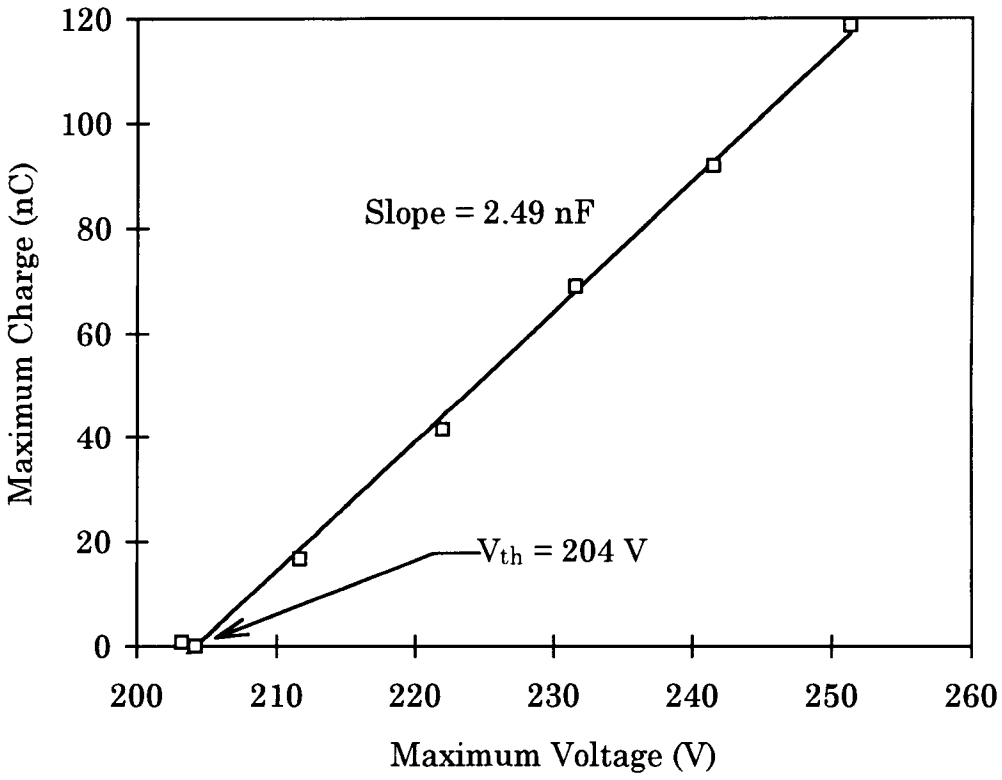

Figure 3.8. Q_{max}-V_{max} curve for a TFEL thiogallate device obtained from Q-F_p curves at room temperature and 1000 Hz.

curve is obtained by collecting a set of Q-F_p curves at various V_{max}'s, and plotting Q_{max} vs. V_{max}. Figure 3.8 shows a Q_{max}-V_{max} curve for a thiogallate device obtained at room temperature and a frequency of 1000 Hz. This device has a physical capacitance of 2.65 nF. There are two important features should be noted in the figure. First, the threshold voltage, V_{th}, is defined as the intercept of the line with the V_{max} axis. This threshold voltage generally agrees well with the optical threshold voltage obtained from a brightness versus a peak voltage (B-V) curve. Second, the slope of the Q_{max}-V_{max} curve is a capacitance which provides important information related to electron emission and capture processes and charge multiplication or impact ionization. A Q_{max}-V_{max} slope greater than the physical capacitance of the insulator is evidence for band-to-band impact ionization, in which electron-hole pairs are created in the bulk region. These induced-holes subsequently drift to the cathode interface. Upon reaching the interface, they recombine very slowly with electrons. A Q_{max}-V_{max} slope less than the physical capacitance of the insulator indicates that the device has insufficient charge transfer, due to interface state injection and perhaps band-to-band impact ionization, for field-clamping.

Obtaining a Q_{max}-V_{max} curve from individual Q-F_p curves, as mentioned above, is an extremely time consuming process. Therefore, it is desirable to generate the Q_{max}-V_{max} curve in a more direct fashion. The following derivation shows how the Q_{max}-V_{max} measurement can be performed from the

measurement of $q_{ext}(t)$ curves as a function of V_{max}.

The instantaneous internal and external charges, $q_{int}(t)$ and $q_{ext}(t)$, are given by Eqs. 3.5 and 3.7, respectively. Substitute Eqn. 3.7 into 3.5 and redefine the external applied voltage to be $v_{ext}(t)$,

$$q_{\text{int}}(t) = \frac{C_i + C_p}{C_i} q_{ext}(t) - C_p v_{ext}(t) . \tag{3.9}$$

Differentiate Eq. 3.8 with respect to $v_{ext}(t)$,

$$\frac{d\left[q_{\text{int}}(t)\right]}{d\left[v_{ext}(t)\right]} = \frac{C_i + C_p}{C_i} \frac{d\left[q_{ext}(t)\right]}{d\left[v_{ext}(t)\right]} - C_p \frac{d\left[v_{ext}(t)\right]}{d\left[v_{ext}(t)\right]} . \tag{3.10}$$

During the falling edge of the applied voltage waveform, the slope of the DE portion of a Q-V curve, shown in Fig. 3.7, is equal to the total capacitance, C_t, of the TFEL stack as seen in the Q-V curve. C_t is given by

$$C_t = \frac{C_i C_p}{C_i + C_t} . \tag{3.11}$$

Thus, during the falling edge (i.e. DE) portion of the applied voltage waveform, the measured capacitance (which is equal to $d[q_{ext}(t)]/d[v_{ext}(t)]$) is equal to C_t. Then if Eq. 3.11 is substituted into Eq. 3.10, for C_t

$$\frac{d\left[q_{\text{int}}(t)\right]}{d\left[v_{ext}(t)\right]} = 0 . \tag{3.12}$$

Equation (3.12) shows that during the falling edge of the applied voltage waveform (i.e. the DE portion), $q_{int}(t)$ is constant and is equal to Q_{max}. Therefore, Q_{max} can be evaluated anywhere in the DE portion of the Q-F_p

curve, i.e.

$$q_{int}(t = \text{DE regime}) = q_{max} \tag{3.13}$$

provided that there is a negligible amount of charge collapse during this

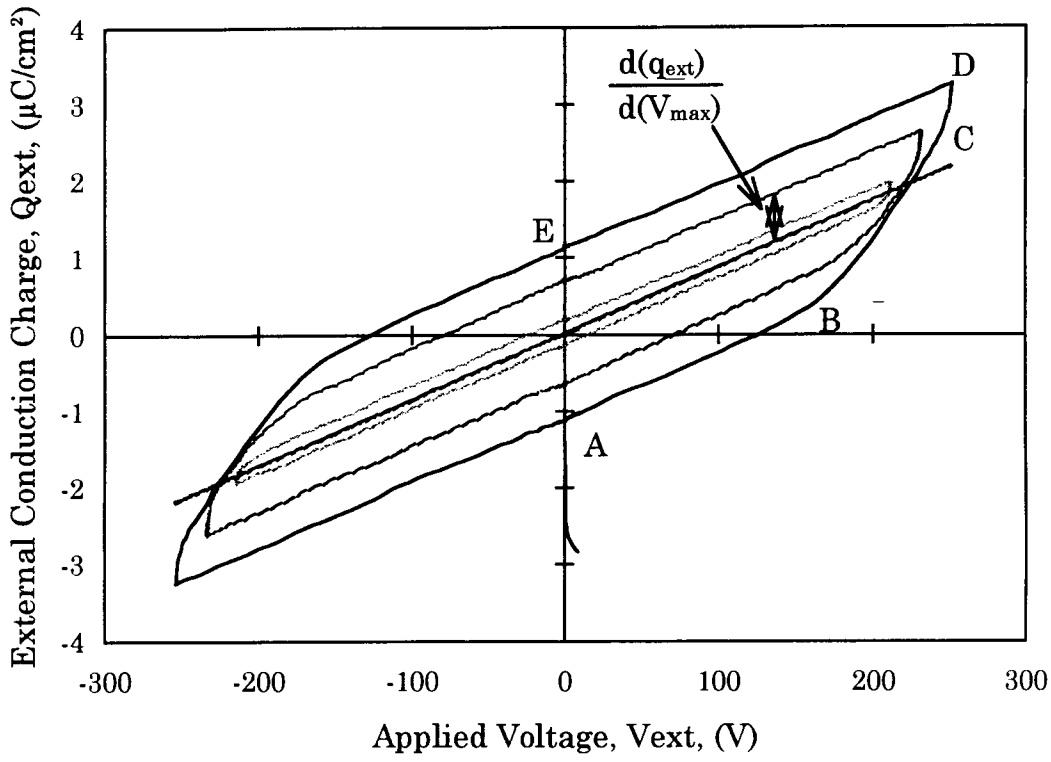

Figure 3.9. Q-V curves for a thiogallate device plotted at three different V_{max}'s.

portion of the applied voltage waveform. The validity condition for Eq. 3.12 is that the Q-F_p curve should have a slope of zero during the DE portion of the applied voltage waveform (see Fig. 3.5). Therefore, the flatness of a Q-F_p curve in the DE regime determines how accurate C_t may be estimated from a C-V or Q-V measurement.

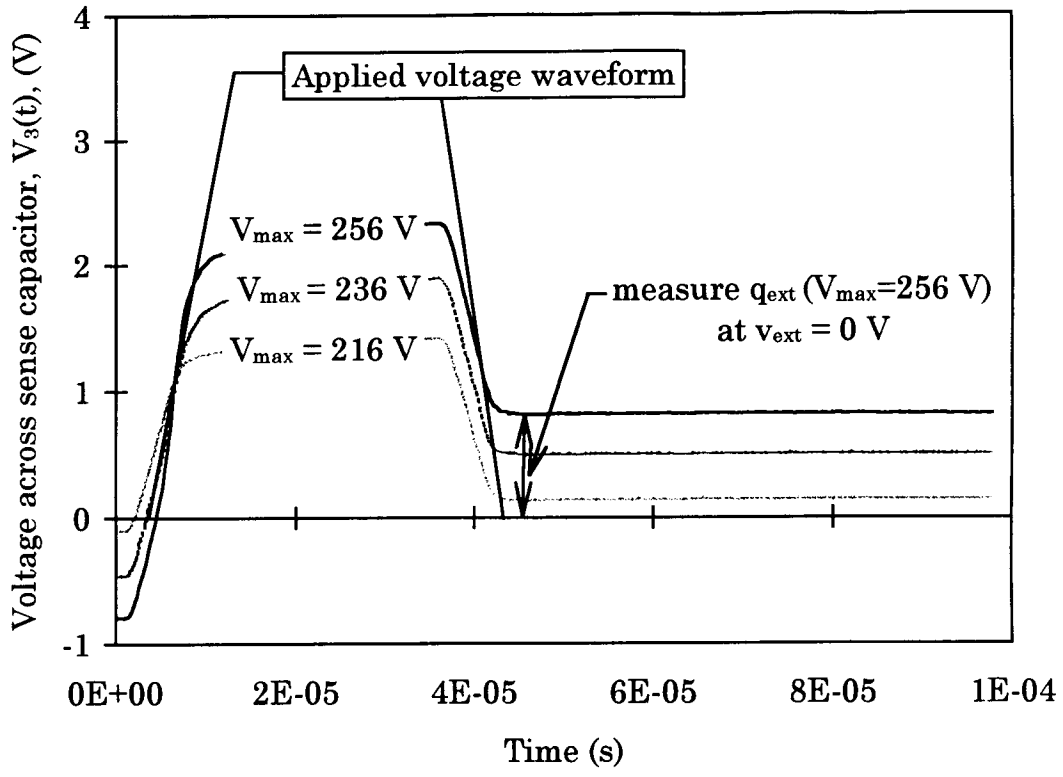

Figure 3.10. Transient voltage across a sense capacitor for three different V_{max}'s.

Since $q_{int}(t)$ equals Q_{max} in the DE portion the applied voltage waveform, substitute Q_{max} into Eq. 3.9 and differentiate it with respect to V_{max},

$$\frac{d[Q_{\max}]}{d[V_{\max}]} = \frac{C_i + C_p}{C_i}\frac{d[q_{ext}(t)]}{d[V_{\max}]} - C_p\frac{d[v_{ext}(t)]}{d[V_{\max}]}. \qquad (3.14)$$

If $v_{ext}(t)$ is evaluated at a constant value of the external applied voltage, the second term in Eq. 3.14 is equal to zero so that

$$\frac{d[Q_{\max}]}{d[V_{\max}]} = \frac{C_i + C_p}{C_i}\frac{d[q_{ext}(t)]}{d[V_{\max}]}. \qquad (3.15)$$

Equation 3.15 shows how the slope of a Q_{max}-V_{max} curve can be obtained from a measurement of $q_{ext}(t)$ with respect to V_{max} at a specific value of V_{ext} in the

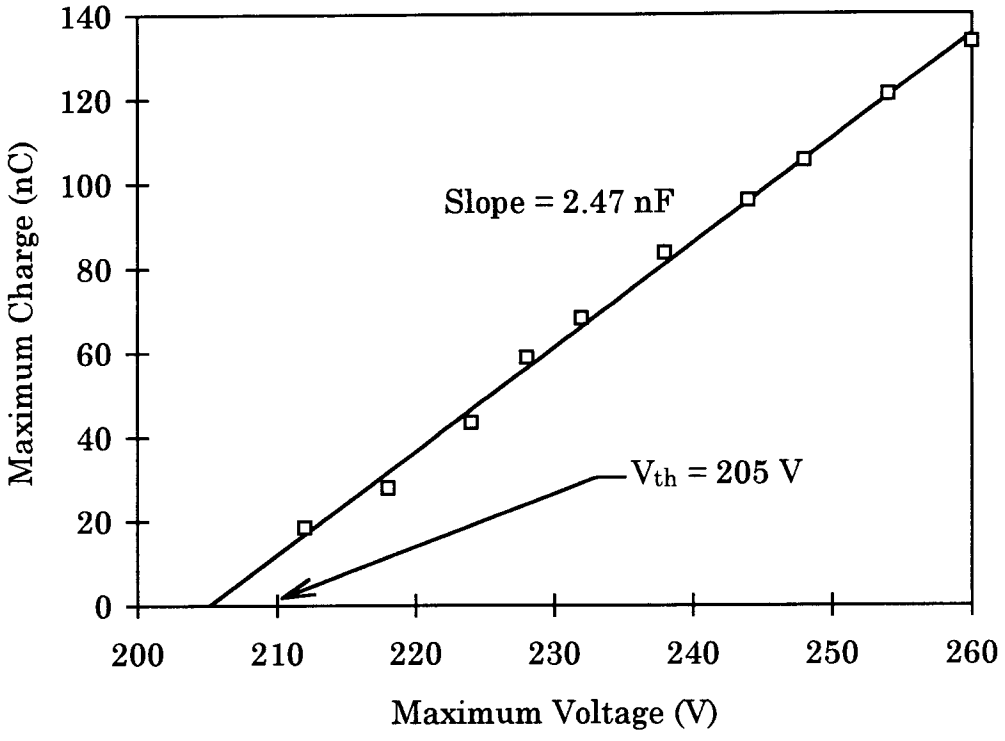

Figure 3.11. Q_{max}-V_{max} curve for a TFEL thiogallate device obtained at room temperature and 1000 Hz.

DE regime. Evaluation of $d[q_{ext}(t)]/d[V_{max}]$ at a constant V_{ext} is illustrated in Fig. 3.9. Using Eq. 3.15, a Q_{max}-V_{max} curve can be measured and plotted directly from a set of $q_{ext}(t)$ curves without the necessity of plotting Q-F_p curves. Figure 3.10 shows the transient voltage across a sense capacitor, C_c, which is connected in series with the TFEL device at three different V_{max}'s.

The value of external charge, $q_{ext}(t)$, used in Eq. 3.15 is evaluated just after (~10μs) the falling edge of a voltage pulse has occurred, as indicated in Fig. 3.10. $q_{ext}(t)$ is evaluated at this time in order to satisfy the requirement that $v_{ext}=0$ and yet minimize the amount of leakage charge decay.

The Q_{max}-V_{max} curve obtained directly from the Q-V measurement is shown in Fig. 3.11. The slope obtained in this figure is 2.47 nF which, to within experimental error, agrees well with the result obtained from Q-F_p curves shown in Fig. 3.8.

Chapter 4 - Comparison of the Electrical Properties of Thiogallate and Evaporated ZnS:Mn TFEL Devices

4.1 Introduction

This chapter presents a comparison of the electrical characteristics of thiogallate and ZnS:Mn TFEL devices grown by evaporation. The device physics operation of yellow-emitting ZnS:Mn TFEL devices is used as a reference point for comparing the performance of thiogallate TFEL devices because ZnS:Mn devices possess the best achieved performance to date, in term of luminance and luminous efficiency.

4.2 Sample Preparation

The basic structure of a TFEL thiogallate device is shown in Fig. 4.1. ALE-deposited aluminum-titanium oxide (ATO) is used as the bottom insulator and sputter-deposited barium tantalate (BTO) is used as the top insulator. ATO is used as the bottom insulator because it has very good stability at high temperature, and it does not affect the properties of the ITO during the insulator deposition process. BTO is used because it has good dielectric properties, i.e., high dielectric constant and electric breakdown strength, and is easy and convenient to deposit. The ZnS underlayer is necessary for achievement of crystallinity and film morphology of the

phosphor layer. A uniform film morphology is desirable to minimize high local field regions.

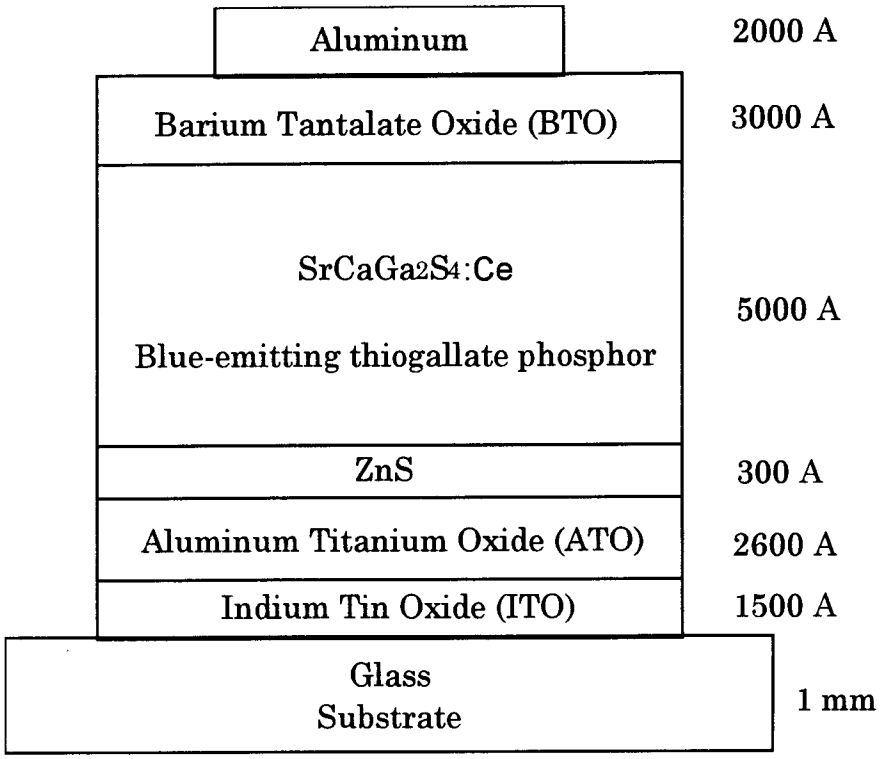

Figure 4.1. Typical thiogallate device structure.

4.3 Experimental Techniques

Electrical characterization of both thiogallate and ZnS:Mn devices is accomplished using C-V and Q-F_p analysis, as discussed in Chapter 2.

4.4 Experimental Results

4.4.1 Capacitance-Voltage (C-V) Analysis

Figure 4.2 is a C-V curve for an evaporated ZnS:Mn TFEL device obtained at three maximum applied voltages. In this figure and subsequent C-V and Q- F_p curves which display three curves, V_{max} is chosen to be approximately 30, 50, and 70 V above threshold. The curves shown in Fig. 4.2 are for a Al positive potential, applied to the Al electrode. First, note that C_t and C_i agree well with that expected from the known thicknesses and dielectric constants of the TFEL stack. Second, notice that the insulator

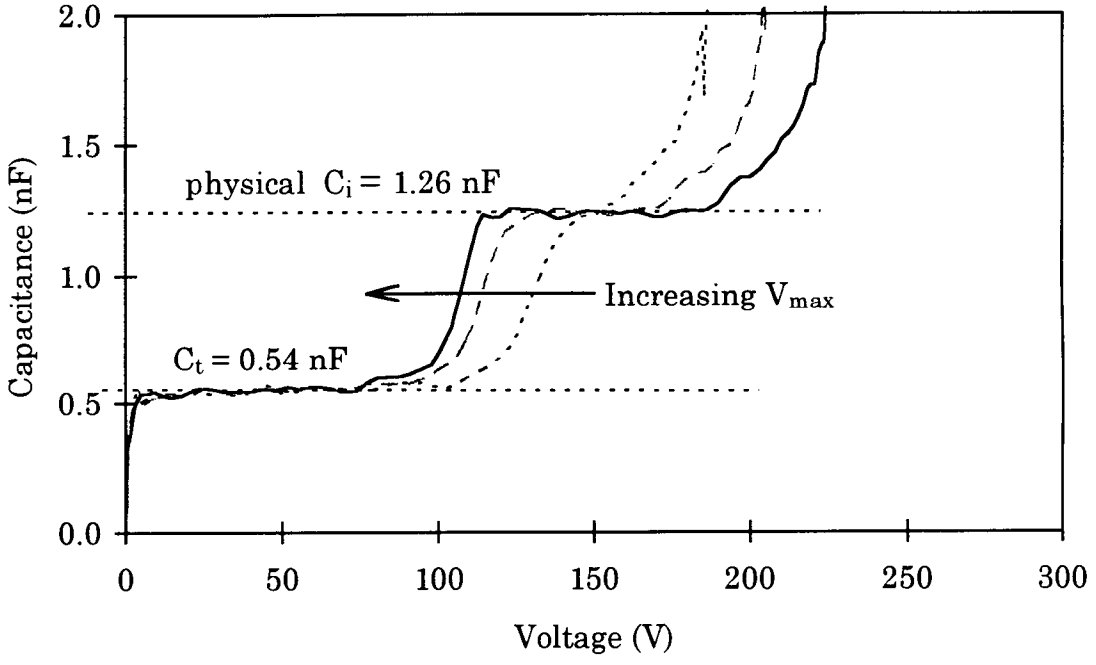

Figure 4.2 C-V curves for an evaporated ZnS:Mn TFEL device. The maximum applied voltage, V_{max}, is 190, 210, 230 V.

capacitance, C_i, is well defined for all of the C-V curves except for the case of V_{max} = 190 V where the applied voltage is very close to that of threshold, in which case C_i is not well established. A C-V curve with a well defined C_i as shown in Fig. 4.2 is evidence for field-clamping. Further, and more conclusive evidence for field-clamping is presented in the next section. Third, note that the C-V curves shift rigidly to lower voltage with increasing V_{max}. Such a rigid shift in the C-V curves to lower voltages is consistent with the build up of polarization charge at the phosphor/insulator interface.

A set of C-V curves for a blue thiogallate TFEL device is shown in Fig. 4.3 for three different V_{max}'s. The C-V curves for Fig. 4.3 are for the positive polarity. In general, C-V curves for thiogallate TFEL devices display some

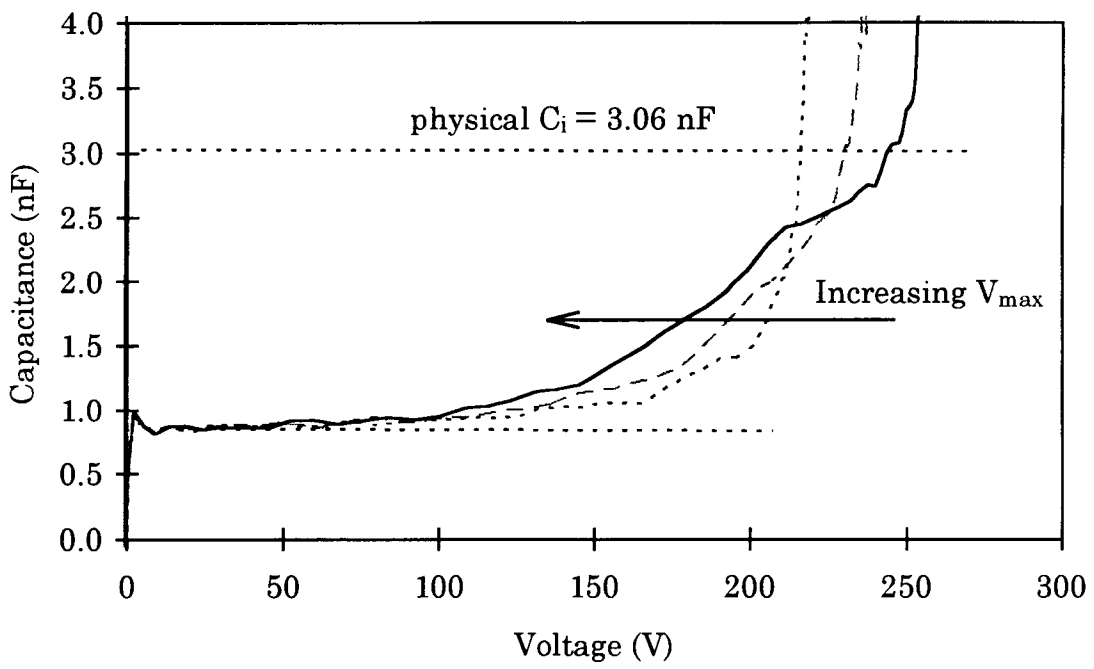

Figure 4.3 C-V curves for a blue $CaGa_2S_4$:Ce TFEL device. The maximum applied voltage, V_{max}, is 220, 240, 260 V.

degree of asymmetry with respect to the voltage polarity. A comparison of Figs. 4.2 and 4.3 indicates significant differences between these sets of curves and that Fig. 4.2 is much more ideal than Fig. 4.3. First, note that while C_t measured in Fig. 4.3 is in good agreement with that expected from the thicknesses and dielectric constants of the TFEL stack, there is no region in the measured C-V curves that corresponds to C_i. In fact, except for the rising portion of the C-V curve near V_{max} (which is not indicative of the real device capacitance), the measured capacitance is always substantially less than C_i. Furthermore, the maximum value of the measured capacitance is larger for larger V_{max}'s; this larger measured capacitance corresponds to the flow of a larger current across the phosphor at larger V_{max}. This fact indicates that the phosphor is only partially breaking down. In fact, Fig. 4.3 does not show any well defined capacitance plateaus in which steady-state is achieved (i.e., steady-state between the rate of the external bias slew rate and the emission rate of electrons giving rise to conduction and a corresponding decrease in the phosphor field). Therefore, the efficiency of this device seems to be inhibited by an insufficient rate of carrier injection. Second, notice that although the C-V curves shown in Fig. 4.3 do shift to decreasing voltages with increasing V_{max}, it is clear that this shift is not rigid. In fact, these C-V curves appear to be almost anchored at V_{to1} (approximately 120 V) and to increase in slope around this anchor point with some distortion of the C-V curve with increasing V_{max}. This anchoring of V_{to1} is attributed to the fact the

some of the carrier injection arises from the emission from bulk trap states, in contrast to exclusively interface state injection in which case the C-V curves shift rigidly. This conclusion is consistent with how this particular TFEL device is processed, i.e. it is prepared under non-ideal deposition conditions which might have resulted in a deficiency of Ga or S in the thiogallate thin films. It is common to find a high concentration of bulk trapping states in sub-stoichiometric semiconductor materials. This resulted in poor performance and brightness (0.44 fL at 40 V above the threshold voltage) for this device.

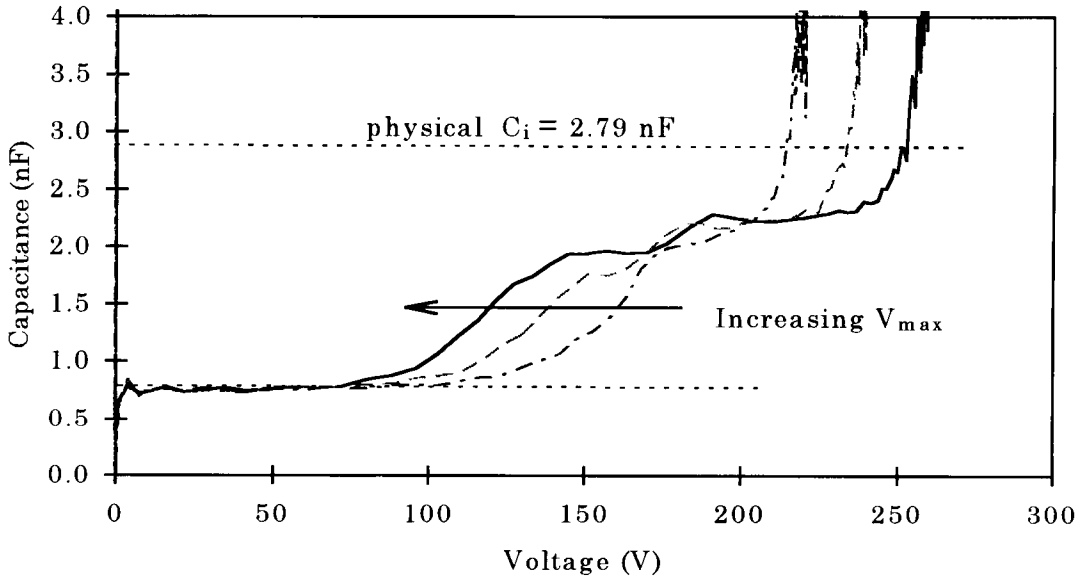

Figure 4.4 C-V curves for a blue $CaGa_2S_4$:Ce TFEL device. The maximum applied voltage, V_{max}, is 220, 240, 260 V.

Another set of C-V curves is indicated in Fig. 4.4 for a thiogallate TFEL device which was processed under improved conditions which resulted

in films close to full stoichiometry and better brightness (1.0 fL at 40 V above the threshold voltage). First, note that the C-V curves shift essentially rigidly with increasing V_{max}. This is consistent with interface state charge injection, similar to that observed for evaporated ZnS:Mn TFEL devices, as indicated in Fig. 4.2, and in contrast to that shown in Fig. 4.3. Second, note that for V_{max} = 240 V and 260 V, there are capacitance plateau regions, indicating steady-state operation, but that these capacitance plateaus are at smaller capacitances than that expected for the insulator capacitance. Thus, field-clamping does not occur for these devices. Again, the performance, such as brightness, of this device seems to be inhibited by the inadequate rate of carrier injection since C_i is not observed in the measured C-V curves.

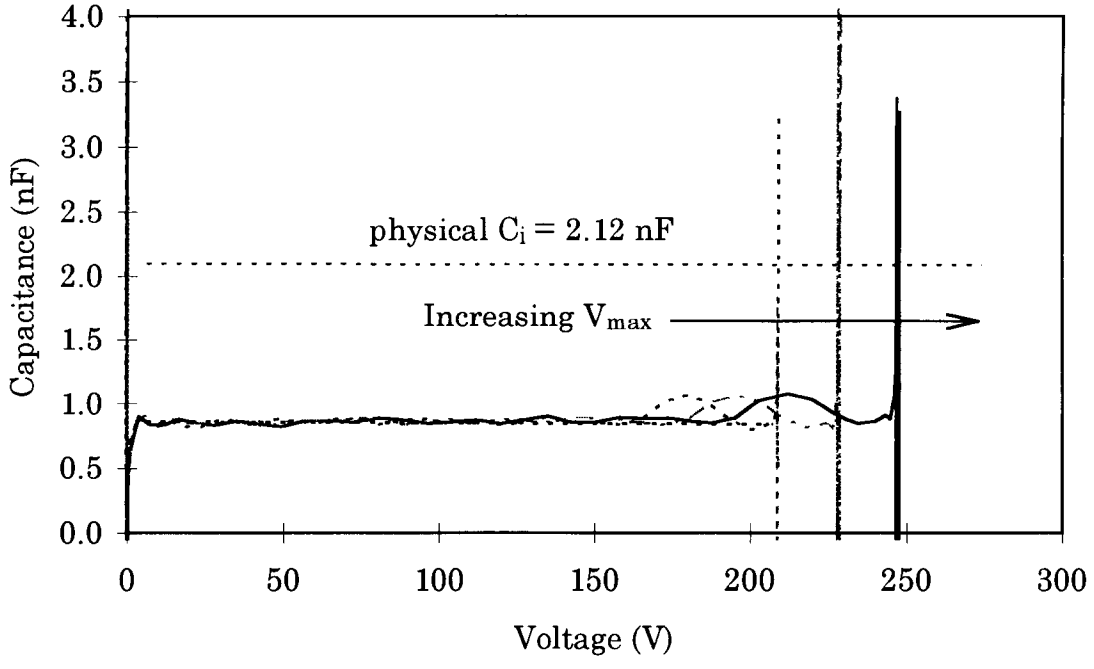

Figure 4.5. C-V curves for a $CaGa_2S_4$ TFEL device in which the phosphor is amorphous because the phosphor was not annealed. V_{max} is 210, 230, 250 V.

Figure 4.5 illustrates C-V curves for an undoped thiogallate TFEL device which was not annealed so that the phosphor is amorphous or, at best, polycrystalline with exceedingly small grains. Three things are worth noting from Fig. 4.5. First, there is very little evidence of a capacitance transition and, therefore, no evidence for a strong breakdown of the phosphor. Presumably, this is associated with the difficulty of charge transport in the amorphous phosphor due to increased scattering and trapping. Second, V_{to1} in Fig. 4.5 occurs at much larger voltages than what is observed for TFEL devices with crystalline phosphors. This is at least partially due to the absence of polarization charge. Third, V_{to1} shifts to greater voltages with increasing V_{max}. This strange behavior is not yet understood. The primary conclusion that can be obtained from Fig. 4.5 is that the phosphor crystallinity is of crucial important to the efficient operation of a TFEL device.

4.4.2 Internal Charge-Phosphor Field (Q-F_P) Analysis

A Q-F_p curve for an evaporated ZnS:Mn TFEL device is shown in Fig. 4.6. This curve is used to compare to the Q-F_p curve shown in Fig. 4.7 for a blue thiogallate TFEL device. From these curves, several distinct differences may be noted. The first obvious difference in the Q-F_p curves given in Fig. 4.7 is that the magnitude of Q_{leak} is much smaller for the thiogallate TFEL

device than it is for the ZnS:Mn TFEL device. The magnitude of the leakage charge depends on the energy depth of the trap states and the magnitude of the phosphor field due to polarization. By comparing the middle curve of Fig 4.6 to the outer curve of Fig. 4.7, it is concluded that the thiogallate traps are deeper than the ZnS:Mn traps since Q_{leak} is much greater for the ZnS:Mn TFEL device when the phosphor polarization fields are comparable in magnitude. The thiogallate TFEL device used for Fig. 4.7 has C-V curves which shifted rigidly to lower voltages, indicating that charge injection in this device is due predominantly to interface state emission. Thus, Q_{leak} is smaller for thiogallate than ZnS:Mn TFEL devices because the interface states from which electron emission occurs are deeper in energy for thiogallate TFEL devices.

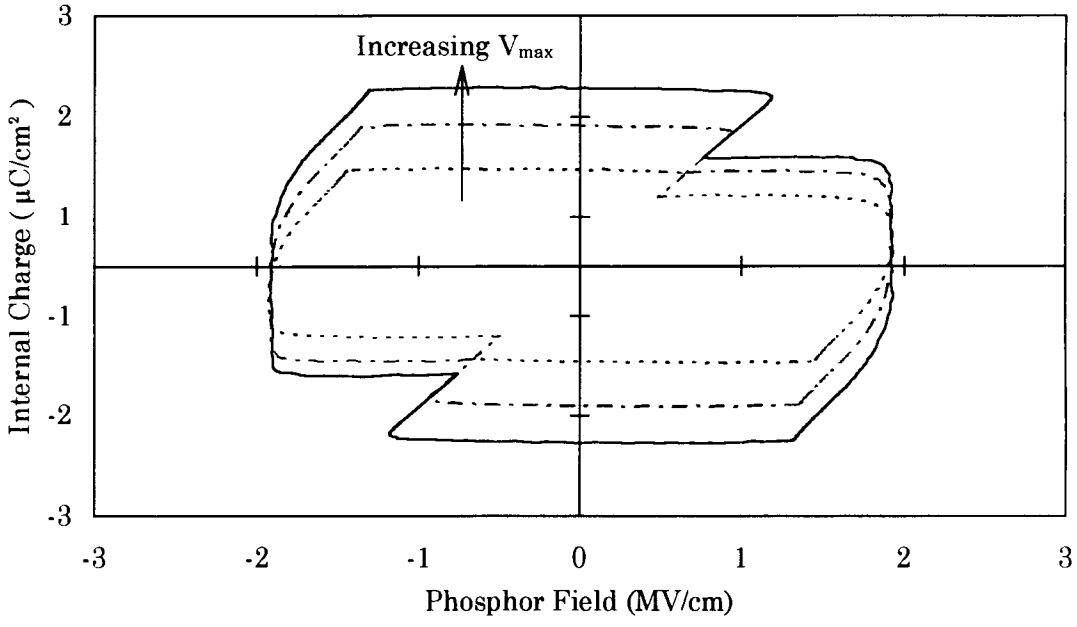

Figure 4.6. Q-F_p curves for a yellow, evaporated ZnS:Mn TFEL device. The maximum applied voltage, V_{max}, is 190, 210, and 230 V.

The second distinct difference between the Q-F_p characteristics of ZnS:Mn and thiogallate TFEL devices is seen in the BC portions of the Q-F_p curve. Figure 4.6 clearly indicates that field-clamping occurs for the evaporated ZnS:Mn device because F_{ss}, as determined by the BC portion of the Q-F_p curve, is a constant which is independent of V_{max}. In contrast, Fig. 4.7 exhibits no such field-clamping and, in fact, shows no evidence for the attainment of steady-state since the Q-F_p curves are never vertical in the BC

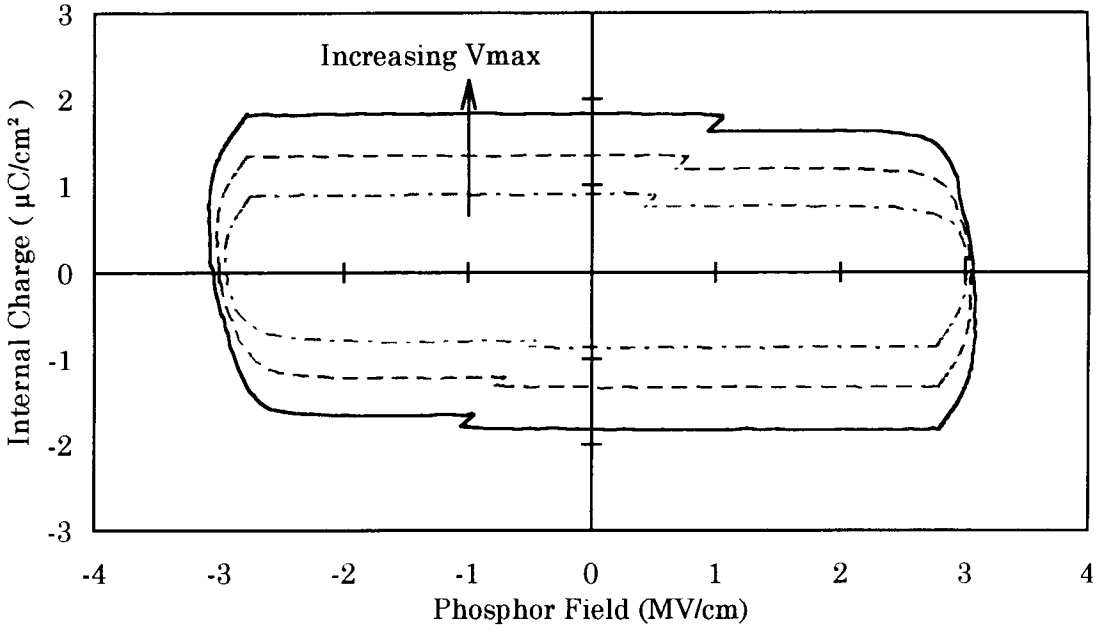

Figure 4.7. Q-F_p curves for a blue $CaGa_2S_4$:Ce TFEL device. The maximum applied voltage, V_{max}, is 220, 240, 260 V.

portion of the Q-F_p curve. Additionally, note that $F_{ss} = F_{clamping} = 2$ MV/cm for the evaporated ZnS:Mn TFEL device whereas $F_{max} = 3.3 - 3.5$ MV/cm for the thiogallate device. The much larger phosphor field observed in Fig. 4.7 also

indicates that the interface states are deeper in energy for the thiogallate TFEL device.

Moreover, notice that the B region of the Q-F_p curve of Fig. 4.7 is rounded and that the BC portion of the curve gradually rises with a gentle slope. This is in contrast to the BC portion of the Q-F_p curve given in Fig. 4.6 which has a sharp corner near B and is vertical from B to C. The shape of the BC portion of a Q-F_p curve provides insight into the interface state density. ZnS:Mn TFEL devices have an interface state density which is very abrupt and exceedingly large. In contrast, thiogallate TFEL devices have a smaller interface density which is deeper in energy and also spread out in energy.

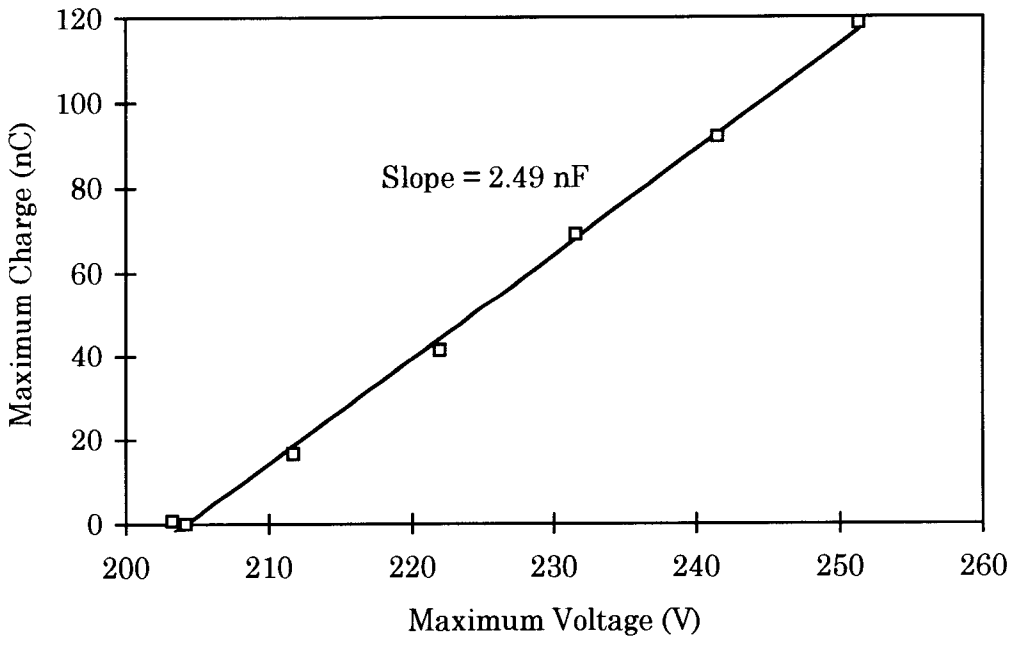

Figure 4.8. A Q_{max}-V_{max} curve for a standard thiogallate TFEL device.

Figure 4.8 shows a Q_{max}-V_{max} curve for a standard thiogallate device. The physical insulator capacitance of this device is 2.65 nF, based on the known thicknesses and dielectric constants of the insulating layers. Note that the slope obtained from the Q_{max}-V_{max} curve, 2.49 nF, is less than that of the physical capacitance. This is evidence that band-to-band impact ionization does not occur in the thiogallate TFEL device. Thus, there are an insufficient number of electrons emitted from interface states for the thiogallate device to achieve strong field-clamping, as observed in Fig. 4.7 which shows no evidence for field clamping in the Q-F_p curves. Unlike the thiogallate device, the slope of the Q_{max}-V_{max} curve of the ZnS:Mn TFEL device is very large, almost double the physical capacitance. Therefore, most of the electrons stored at interface states in ZnS:Mn TFEL device arise from electron multiplication in the bulk region due to band-to-band impact ionization, resulting in a strong field-clamping for the ZnS:Mn device, as shown in Fig. 4.6.

4.5 Conclusion

The electrical characteristics of evaporated yellow-emitting ZnS:Mn and blue-emitting thiogallate devices are compared and contrasted using C-V and Q-F_p analysis. Evaporated ZnS:Mn TFEL devices exhibit nearly ideal electrical characteristics which are dominated by strong field-clamping due electron multiplication via band-to-band impact ionization. In contrast, blue-

emitting thiogallate TFEL devices do not exhibit band-to-band impact ionization and field-clamping. The thiogallate interface states are deeper in energy than those of ZnS:Mn TFEL devices. Thiogallate devices also exhibit a very small leakage charge compared to that of ZnS:Mn TFEL devices. This is a desirable feature since less leakage charge implies greater polarization charge, which aids in reducing the turn-on voltage required for the onset of electron emission from the interface.

The results of C-V and Q-F_p measurements suggest that the EL performance of the $CaGa_2S_4$:Ce blue phosphor could be improved if more carrier injection can be provided from the phosphor/insulator interface by an increase in the interface state density and the presence of band-to-band impact ionization in the bulk region.

Chapter 5 - Characterization of Thiogallate Devices; Evidence for Positive and Negative Space Charge Generation in the Phosphor

This chapter presents the results of optical and electrical characterization of thiogallate devices which are fabricated in various ways in order to investigate the mechanisms that result in device improvement. Evidence is provided for the existence of both positive and negative space charge in the phosphor under steady-state operation. The results discussed in Chapter 4 indicate that the EL performance of the $CaGa_2S_4$:Ce blue phosphor is not ideal due to insufficient carrier injection, low interface state densities, the absence of band-to-band impact ionization, and the deficiency of Ga or S in the thiogallate thin films which gives rise to trapping and scattering. The development of blue thiogallate phosphors has been pursued in order to obtain an increased brightness. Some of these development efforts include: varying the process conditions, varying the phosphor thickness, employing metal injection layers, and doping the thiogallate phosphor.

5.1 Effects of Process Parameters on Thiogallate Device Operation

To improve the performance of the thiogallate device, various process parameters are investigated in order to obtain optimal process conditions for

increased brightness. These improvements often include improving carrier injection from the phosphor/insulator interface and/or improving the crystallinity of the phosphor layer. The process parameter variations investigated involve: oxygen doping, substrate temperature, deposition power, and deposition pressure. From experimental results, it is observed that oxygen doping is the most effective parameter for improving the device performance of thiogallate devices.

EL devices fabricated with oxygen doping during deposition of the phosphor layer show better performance than ones made with no-oxygen doping. Major improvements, such as increased brightness, higher efficiency, lower threshold voltage, and smaller subthreshold turn-on (ΔV) are obtained.

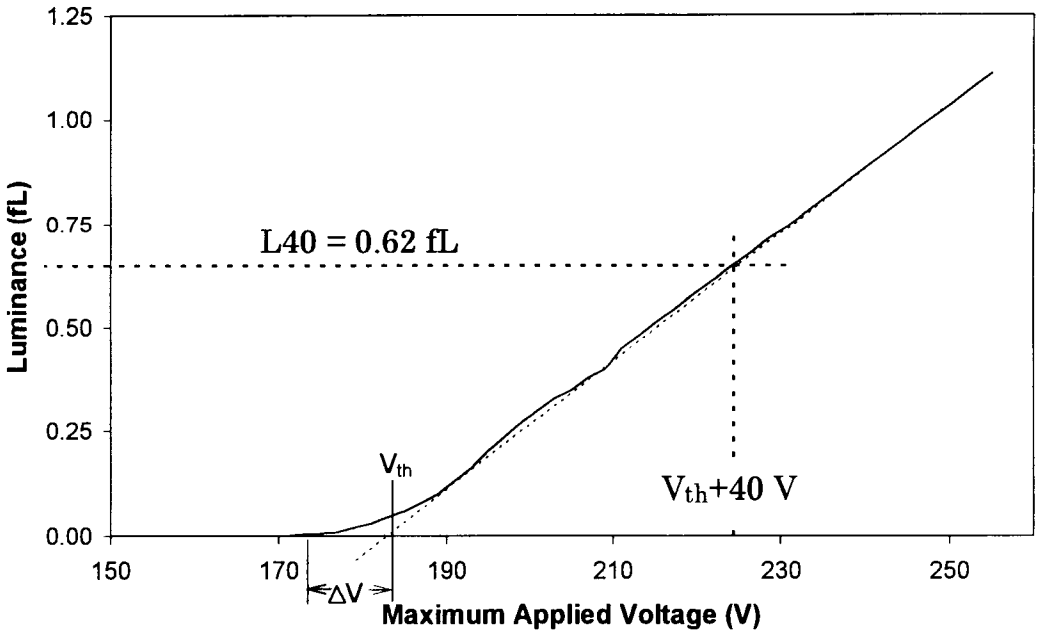

Figure 5.1 Typical B-V curve for a thiogallate device.

Subthreshold turn-on is defined from the B-V curve shown in Fig. 5.1. With oxygen doping, ΔV could be reduce from 10~12 V to 1~4 V. To examine the electrical characteristics of the oxygen doped device versus the non-oxygen doped device, C-V and Q-F_p measurements were employed.

C-V curves for oxygen doped and undoped devices, respectively, are shown in Figs. 5.2 and 5.3. These plots clearly exhibit differences. Figure 5.2 shows that the oxygen doped device possesses a steep slope in the transition regime, a rigid-shift to lower turn-on voltages with increasing V_{max}, and a well-defined effective capacitance plateau in which steady-state

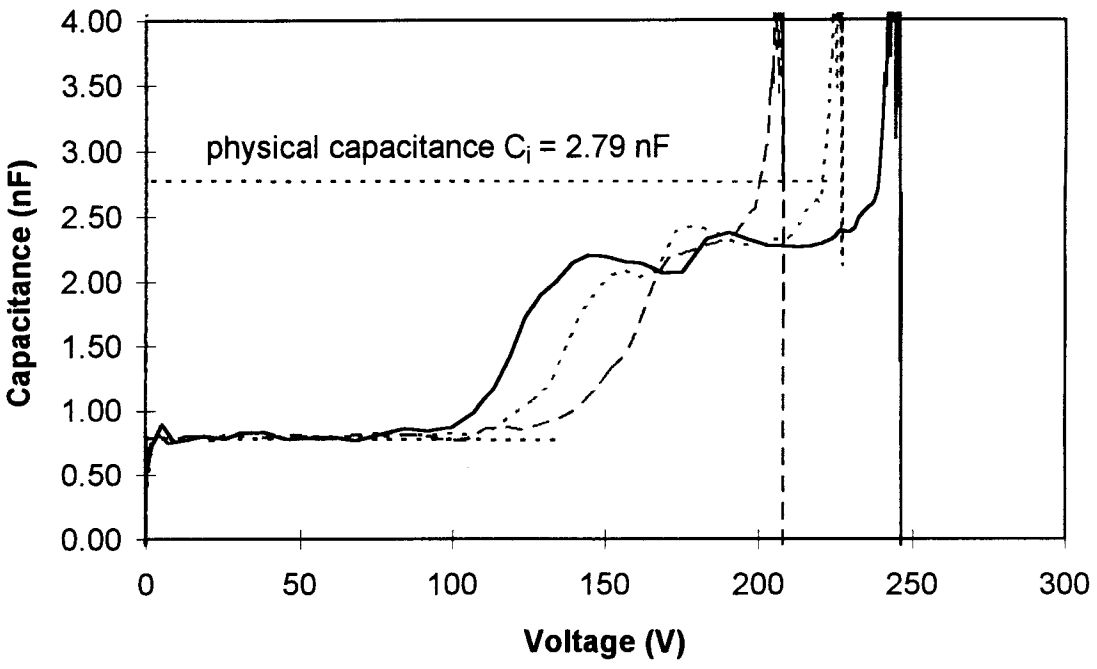

Figure 5.2. Thiogallate device with oxygen doping.

is achieved. In contrast, Fig. 5.3 shows C-V curves with a shallow transition region slope, a non-rigid shift with higher V_{max}, and no well-defined region for the effective insulator capacitance, C_{eff}. In general, it is observed that a device with no well-defined region for C_{eff} exhibits poor performance (e.g. low brightness). The shallow transition slope shown in Fig. 5.3 indicates that

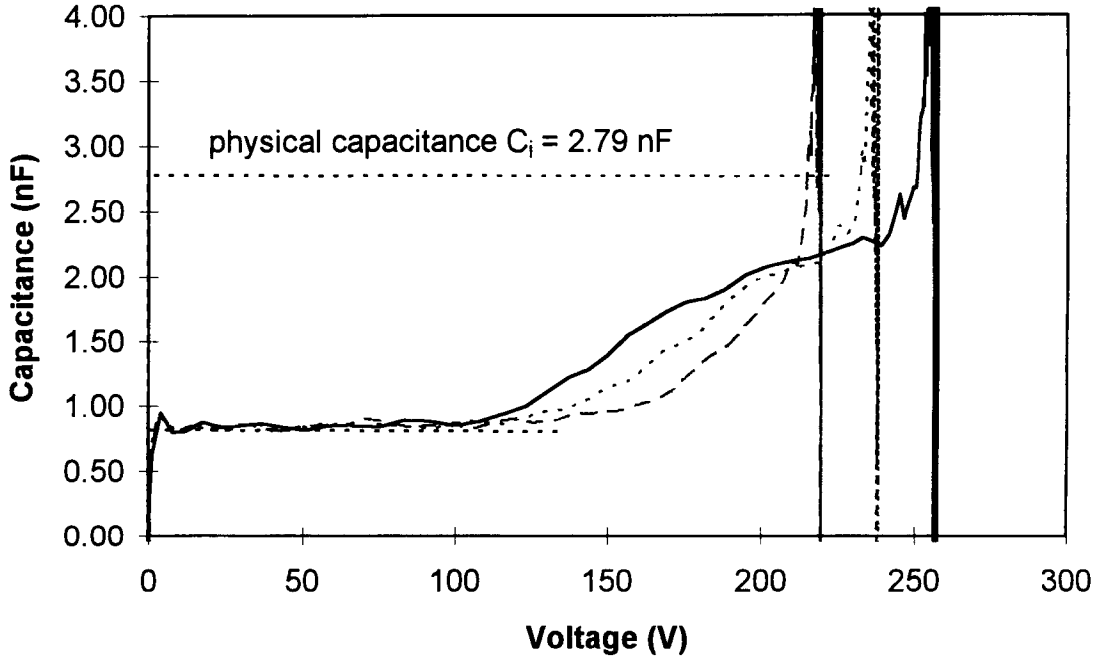

Figure 5.3. Thiogallate device with no oxygen doping.

the undoped device has a lower density of pre-clamping interface states compared with to that of the oxygen-doped device. The non-rigid shift of the

C-V curve for the undoped device suggests that some of the carrier injection arises from the emission of the bulk trap states. These trap states may have resulted from a deficiency of Ga or S in the thiogallate thin film. The rigid-shift observed in Fig. 5.2 suggests that oxygen may have substituted or compensated for S vacancies. This, in turn, would reduce the number of trap states which could contribute carriers to the conduction band, and would also reduce trapping and scattering in the phosphor film.

Devices prepared at high deposition temperature and power showed poor brightness, efficiency, and shallow turn-on characteristics. C-V curves obtained for these devices are similar to that shown in Fig. 5.2; the transition slope is shallow, the shift is non-rigid, and there is no well defined C_{eff} region. These thiogallate films are assumed to be deficient of Ga and S under these processing conditions. However, by lowering either the deposition temperature or the power while keeping other process parameters the same, the device performance showed significant improvement.

Variation of deposition pressure has no effect on C-V curves, but Q-F_p plots show a slight reduction of the phosphor field and conduction charge with increasing deposition pressure. However, the brightness and efficiency are improved with increasing deposition pressure. The dynamic range of the deposition pressure test was not very large. Therefore, its effects on the device performance is not known to any degree of confidence.

5.2 Variation in the Phosphor Thickness and Evidence for Positive Space Charge Generation in the Phosphor

The purpose of this experiment is to investigate the effects of phosphor thickness variations on the optical and electrical device operation. The experiment is performed by measuring the B-V and the Q-F_p curves for a set of thiogallate devices in which the phosphor thickness varied from 4070 A to 5625 A. A B-V plot is used to evaluate the brightness and threshold voltage versus the phosphor thickness, and a Q-F_p plot is used to investigate the effects of phosphor thickness on the phosphor field and conduction charge. The experimental results are summarized in Fig. 5.4. The optical results

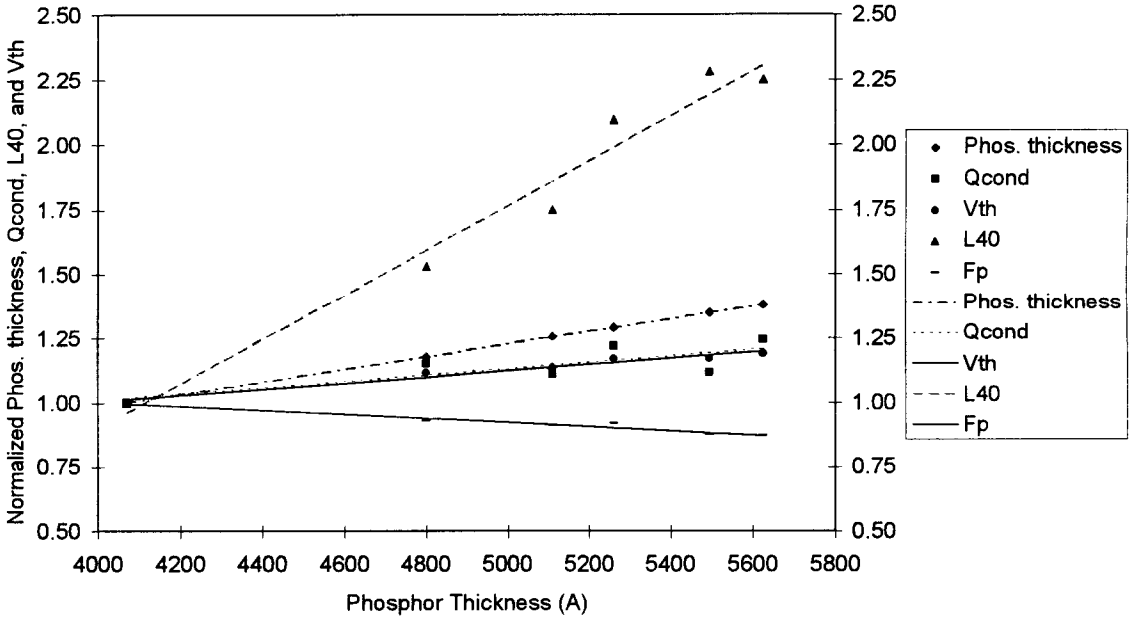

Figure 5.4. Experimental results for the variation in phosphor thickness.

obtained from the B-V curve consists of the brightness at 40 V above the threshold voltage, L40, as shown in Fig. 5.1, and the threshold voltage, V_{th}. The conduction charge and phosphor field shown in Fig. 5.1 are obtained from Q-F_p curves. The experimental results show that with increasing phosphor thickness the brightness increases noticeably, the threshold voltage and the internal conduction charge increase slightly, whereas the maximum attainable phosphor field for a given over voltage decreases.

The observed increase in the threshold voltage is very predictable since the electric field is inversely proportional to the phosphor thickness; therefore, a larger applied voltage is required to attain the same high field.

The improvement in brightness may be attributed one of two possible contributions: (1) the thicker the phosphor the larger the number of luminescent centers available for excitation; (2) conduction charge increases with increasing thickness, as shown in Fig. 5.5. It would appear that contribution (1) is more likely since the increase in conduction charge is much less than the increase in brightness with increasing phosphor thickness.

The conduction charge increase with increase in phosphor thickness could be due to a modification of the interface state density or distribution or due to bulk trap state emission. Changing the phosphor thickness is very unlikely to increase the interface state density unless annealing effects occur which enhance interface restructuring; the thicker the phosphor, the longer

the device remains in the hot sputtering chamber and, consequently, the longer duration of annealing during deposition. Since the substrate temperature during deposition is approximately 50-80°C whereas the post-deposition annealing temperature is 800°C, it seems unlikely that there is much of a perturbation of the interface state density due to annealing during the deposition. It seems more pausible that the increase of conduction charge with increasing phosphor thickness is not associated with the interface but mainly is due to emission from bulk traps. This bulk trap emission is possibly due to Ga or S deficient sites in the phosphor which give rise to the positive space charge generation in the phosphor layer under a high field operation by either field emission or impact ionization. Positive space charge generation in the phosphor bulk is consistent with a reduction in the phosphor field with increasing phosphor thickness, as discussed below.

The observed experimental trends of decreasing phosphor field and increasing threshold voltage with increasing phosphor thickness is rather contradictory to the idea of energetic impact and excitation of luminescent centers since one would expect electrons to become less energetic at a lower phosphor field. This problem may be resolved by recognizing that the measured field is an average field. Therefore, it inaccurately represents the energy of transporting electrons inside the phosphor. The positive space charge generation model, as shown in Fig. 5.5, helps to resolve these difficulties.

In Fig. 5.5, the space charge is assumed to be uniformly distributed throughout the phosphor length. As shown in the figure, the existence of positive charge inside the phosphor causes a downward bending of the energy bands; the higher the concentration of positive space charge the more bending observed. The positive space charge decreases the phosphor field as one moves from the negatively biased to the positively biased interface. Thus, the electrons traveling near the cathode interface are most effective in exciting luminescent impurities since they experience the largest phosphor

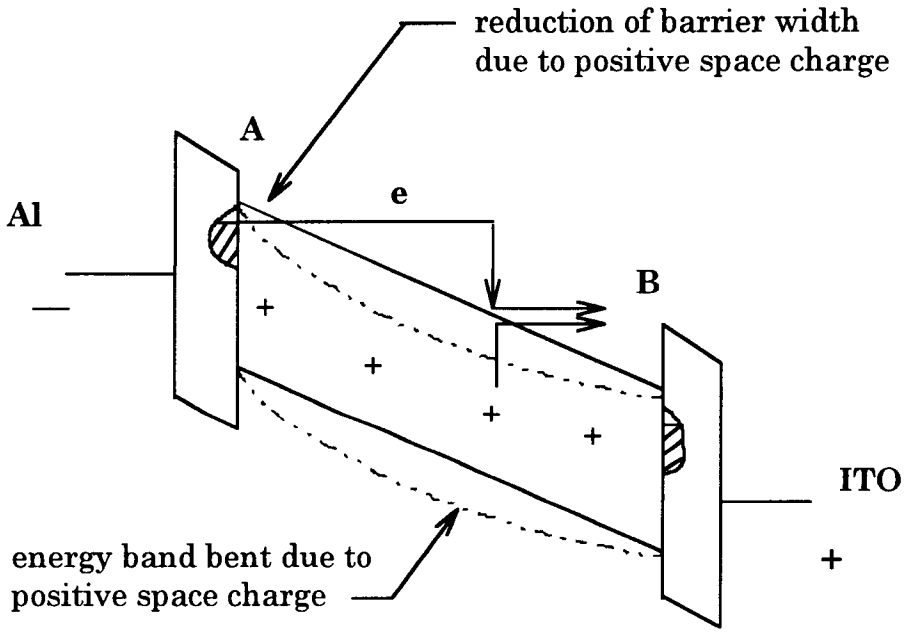

Figure 5.5. Energy band bending due to the existence of positive space charge in the phosphor layer.

fields. The phosphor field is lower near the anode interface. Therefore, anode electrons should be cooler and, consequently, bombard the insulator with lesser force. This subsequently improves the lifetime of the TFEL device due to less damage at the phosphor/insulator interface. Due to the band bending shown in Fig. 5.5, the barrier width decreases with increasing positive space charge. Therefore, less average phosphor field is needed to inject interface electrons into the conduction band. This could contribute to the reduction of the phosphor field, as shown in Fig. 5.4. However, it is more likely that the reduction in the phosphor field seen in Fig. 5.4 is simply due to the fact that there is a reduction in the average field with increasing positive space charge.

In summary, the reduction of the phosphor field and the increase in the conduction charge seem to be related to an increase in the amount of positive space charge generation via bulk trap ionization. The concomitant increase in brightness with increasing phosphor thickness is attributed to the increased number of luminescent impurities present in a thicker phosphor layer. However, an increase in phosphor thickness requires an increase in threshold voltage, which is undesirable since it is requires more complicated circuitry to drive the flat panel display and it is costly to build.

5.3 Metal-Injection Layers and Evidence for Negative Space Charge Generation in the Phosphor

The goal of this section is to present a study of the electrical characteristics of thiogallate phosphor TFEL devices with metal injection layers. Evidence for the existence of negative space charge generation in the phosphor are obtained experimentally from Q-F_p measurements. The purpose of the metal-injection layer is to increase the conduction charge by

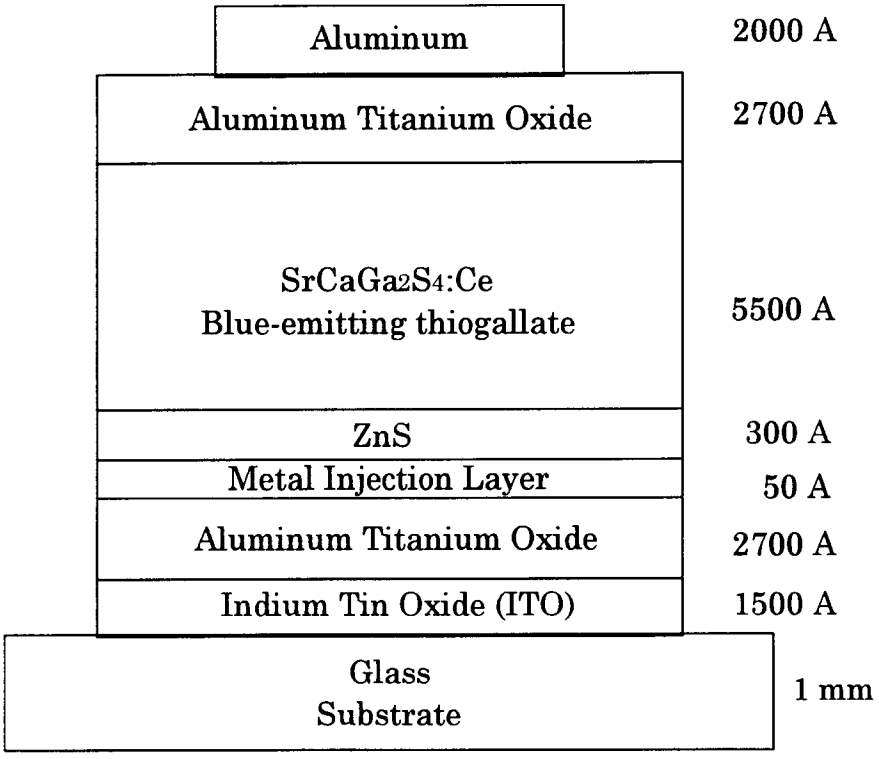

Figure 5.6. Typical EL thiogallate device with a metal injection layer.

modifying the interface state density at the phosphor/insulator interface. The increase in conduction charge gives rise to an increase of the internal current density and, consequently, improves the probability of impact excitation of luminescent impurities which, in turn, improves the device performance.

Figure 5.6 shows how the stack structure of the metal-injection thiogallate devices is fabricated. The metal-injection layer is sandwiched between the bottom insulator (ATO) and the ZnS layer. Figure 5.7 shows energy band diagrams of a standard and a metal-injection layer device under equilibrium conditions which indicates how the metal-injection layer may have improved the interface state density at the metal-injection interface.

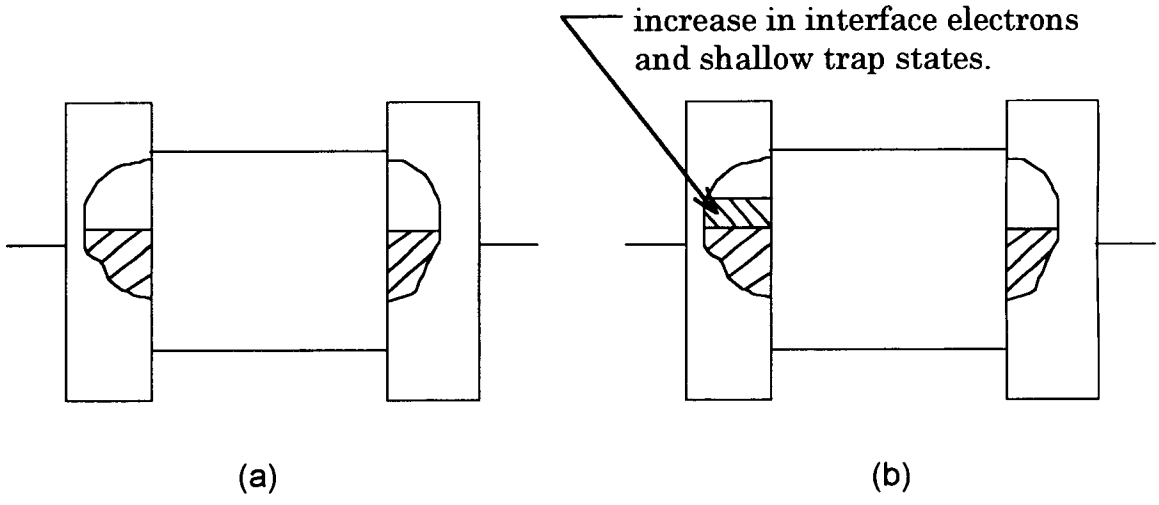

Figure 5.7. Interface state density is modified due to the presence of a metal-injection layer:(a) standard EL device and (b) EL device with metal-injection layer.

Various metals were investigated but, so far indium is the most promising metal for improving the thiogallate TFEL device performance in terms of brightness and phosphor conduction charge. Therefore, this chapter

Threshold voltage, luminescence at 40 V above the threshold, and efficiency of TFEL devices with and without indium-injection layers.

Sample	V_{th} (V)	L40 (fL)	efficiency (lm/W)
standard	194	0.78	0.018
with 29 A of indium	176	0.95	0.023
with 49 A of indium	187	0.95	0.020

mainly concentrates on a discussion of indium-injection devices. The optical results of indium-injection devices are summarize in Table 2.1, which indicates that the indium-injection devices exhibit better device performance (i.e. higher brightness and efficiency, and lower threshold voltage) than that of the standard device:

C-V and Q-F_p analysis is employed in order to examine the mechanisms that result in device improvement. C-V curves for a standard and an indium-injection device, respectively, are shown in Figs. 5.8 and 5.9. First, note from Fig. 5.8 that the C-V curves shift essentially rigidly with increasing V_{max}. Second, the flat portion of the C-V curves indicates that steady-state is achieved and that this device approaches ideal operation.

However the effective capacitance, C_{eff}, is still lower than the physical insulator capacitance. This indicates that the electron emission from the interface is still not high enough to completely shunt the phosphor capacitance. Therefore, the phosphor is only partially broken down. Third, the C-V curve in Fig. 5.8 shows evidence of overshoot in the steady-state region. This overshoot is evidence for the existence of space charge generation or charge multiplication inside the phosphor layer. This space charge may be due to ionization of traps in the phosphor. The shape of this C-V curve can be explained as follows. Initially, there is a large numbers of phosphor traps which are filled with electrons When interface electrons are initially emitted from the interface, they impact ionize these traps, creating charge multiplication within the phosphor layer. During the rising edge of the overshoot, the total phosphor conduction current is a combination of electrons emitted from the interface and from electrons ionized from the trap sites. Beyond the peak of the overshoot, most of the traps are ionized. Therefore, there is a gradual reduction of the ionization charge and, consequently, a decrease of conduction current. When all the traps have been ionized, the charge multiplication ceases and the remaining current arises essentially from interface emission. This occurs in the flat portion of the C-V curve following the overshoot period.

A set of C-V curves for a thiogallate device with an indium-injection is shown in Fig. 5.9. Note that this set of C-V curves also exhibits a rigid shift

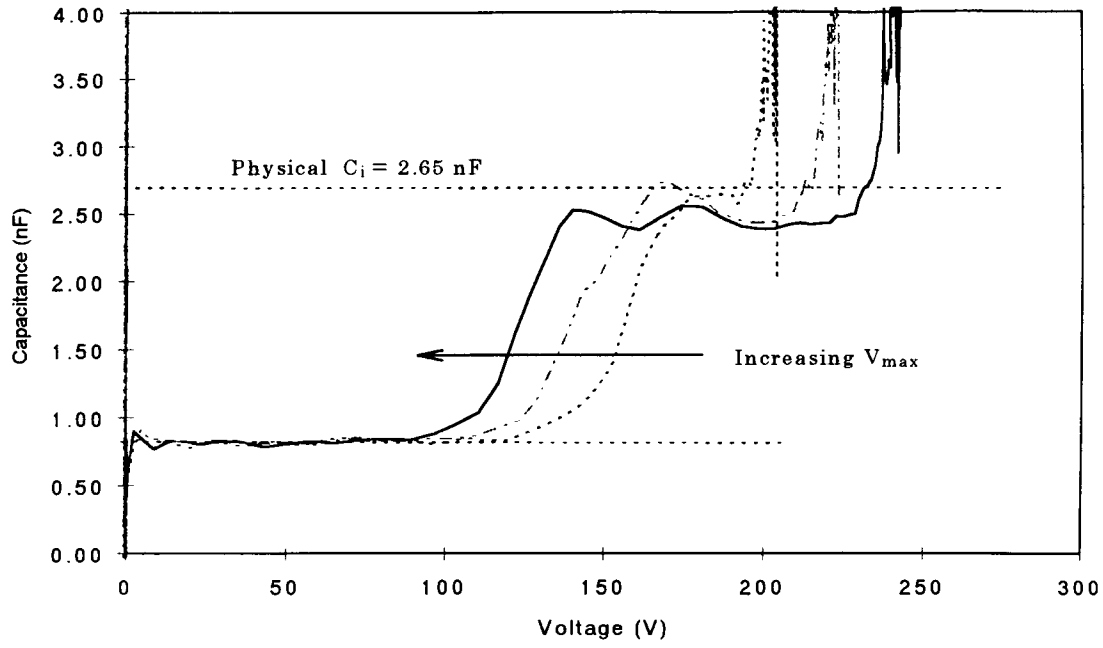

Figure 5.8. C-V curves for a standard TFEL thiogallate device.

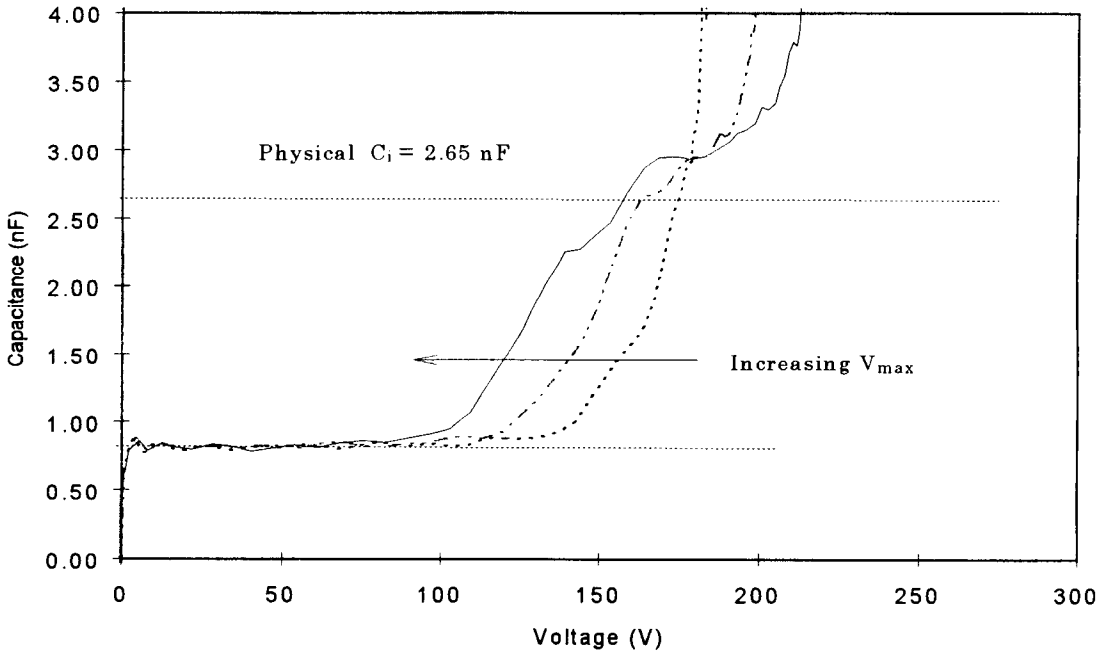

Figure 5.9. C-V curves for a TFEL device with a 29 A indium-injection layer.

to lower turn-on voltage with increasing V_{max}. A comparison of Figs. 5.8 and 5.9 indicates that there is a significant difference between the effective capacitance of these devices. In Fig. 5.9, C_{eff} is much larger than the physical insulator capacitance, i.e. $M > 1$. This indicates that space charge generation exist in the phosphor layer. Also the charge multiplication is persistent with ramping of the applied voltage, i.e. the curve keeps increasing or saturates to a constant value; in contrast, the capacitance decreases after reaching a peak for the standard device.

$Q\text{-}F_p$ curves for a standard and an indium-injection layer device, respectively, are shown in Figs. 5.10 and 5.11. There are significant differences between devices. First, note that the conduction charge is much larger for the indium injection device than for the standard device. This suggests that indium has modified and increased the interface state density at the phosphor/insulator interface and, consequently, increased the conduction charge. Second, Fig. 5.10 shows insufficient charge injection from the interface which leads to $M<1$, whereas, $M>1$ for the $Q\text{-}F_p$ curves observed in Fig. 5.11 and the vertical portion of the $Q\text{-}F_p$ curves consistently have an inward bending. This inward bending is an indication of charge multiplication in the phosphor and is consistent with the C-V characteristics observed in Fig. 5.9, which shows that C_{eff} is much greater than the physical insulator capacitance. Third, a distinctive difference between Figs. 5.10 and

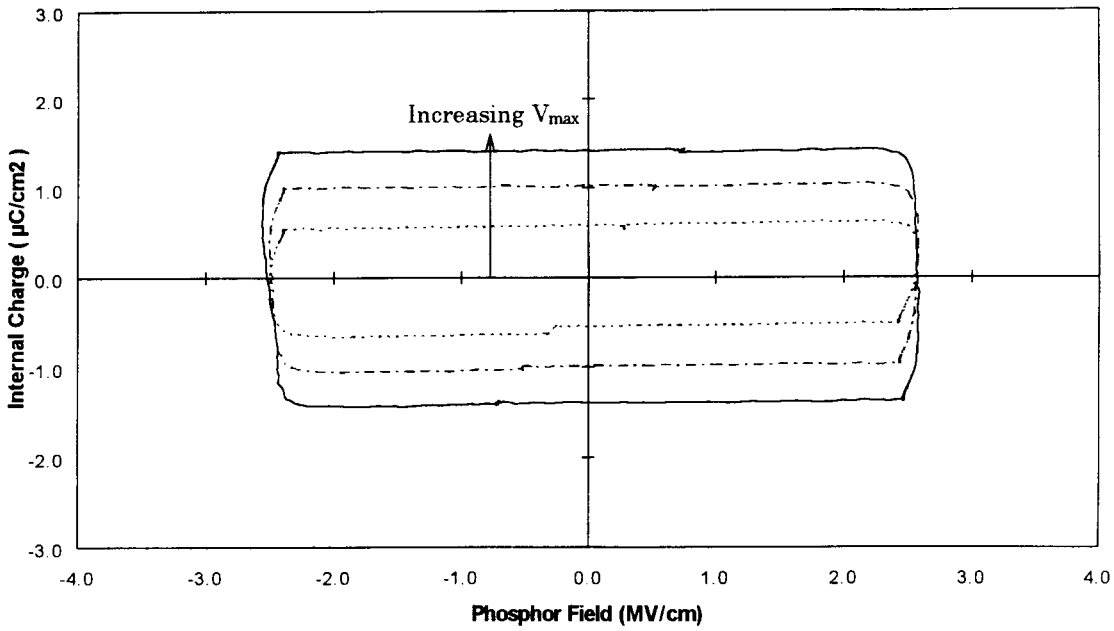

Figure 5.10. Q-F_p curves for a standard TFEL thiogallate device

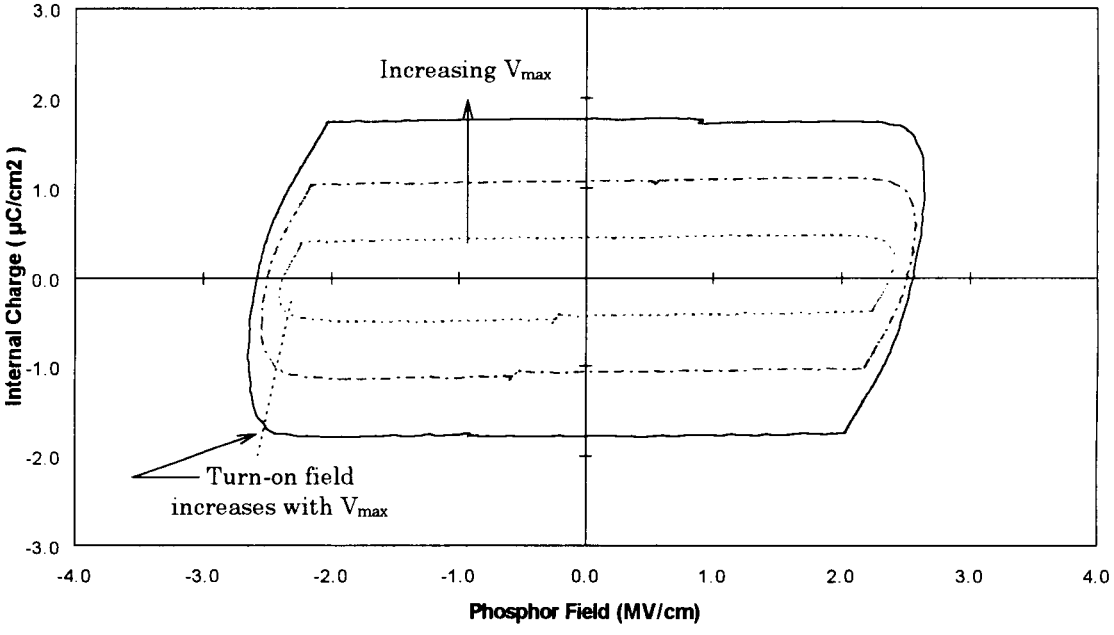

Figure 5.11. Q-F_p curves for a TFEL device with a 29 A of indium-injection layer.

5.11 is the increase of the turn-on field with increasing V_{max} for the indium-injection device. In contrast, the standard device exhibits close to field-clamping behavior in its Q-F_p characteristics.

The positive space charge model discussed previously cannot explain this phosphor field expanding phenomenon because positive space charge leads to a reduction of the phosphor field due to the downward bending of the energy bands and, subsequently, a reduction of the barrier width. To explain the observed increase of the turn-on field with increasing V_{max}, a negative space charge is proposed. The negative space charge model is shown in Fig. 5.12.

The negative space charge model is distinctly different than to that of the positive space charge discussed previously. Due to the existence of

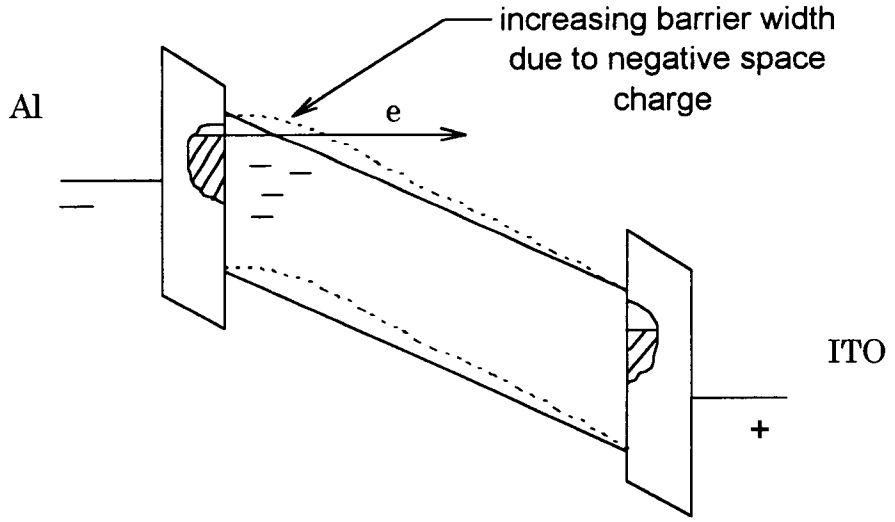

Figure 5.12. Modification of the energy bands due to the existence of negative space charge.

negative space charge in the phosphor near the cathode interface, the energy bands bend upward, thereby lowering the electric field in the region near cathode electrode. This upward bending increases the barrier width of the interface electrons and, subsequently, a larger phosphor field is required to inject interface electrons into the conduction band. As V_{max} increases, more and more negative charge is trapped in the phosphor near the interface due to the increase of conduction charge. This pile up of negative charge subsequently reduces the cathode field and increases the barrier width. The existence of negative space charge in the phosphor is attributed to the small interface state density of thiogallate device which, therefore, does not require a large number of electrons to fill up all of these states. This small interface state density couples with an increase of conduction charge due to the contribution of the indium injection layer, creating a pile up of negative space charge in the phosphor in the vicinity close to the phosphor/insulator interface.

The experimental results indicate that the incorporation of an indium-injection layer contributes to an increase of the conduction charge by modifying the interface state density at the phosphor/insulator interface. This gives rise to an increase of the internal current density which, consequently, improves the probability of impact excitation the luminescent impurities. The indium-injection layer results in more filled shallow traps which, in turn, reduce the required threshold voltage, as shown in Table 2.1.

Chapter 6 - TFEL Variable Temperature and Aging Studies

6.1 Introduction

This chapter presents the results of a short-term aging study and an investigation of the temperature-dependent characteristics of TFEL thiogallate devices. Aging studies are performed to determine aging properties and mechanisms on the device operation of TFEL thiogallate devices in term of brightness and electrical characteristics. The aging experiments are performed by monitoring the C-V, Q-F_p, Q_{max}-V_{max}, and B-V characteristics as a function of time at room temperature. Variable temperature testing of blue thiogallate TFEL devices is performed to determine the effects of temperature on the performance of these devices in term of luminance and electrical characteristics. These experiments are accomplished by monitoring the luminance, conduction charge, C-V, Q-V, Q-F_p, and Q_{max}-V_{max} characteristics as a function of temperature.

6.2 Aging Experimental Results

The experimental trends of Q_{max}-V_{max} curves as a function of aging time for a positive applied voltage pulse to the Al electrode of a standard blue thiogallate TFEL device are shown in Figure 6.1. First, note that the Q_{max}-V_{max} curves shift rigidly to higher threshold voltage with aging time and that

and their slope remains unchanged and is less than that of the physical insulator capacitance. The rigid-shift of Q_{max}-V_{max} is an indication of an aging mechanism associated with the modification of the insulator/phosphor interface states, not the bulk phosphor region. This rigid-shift of the Q_{max}-V_{max} curve to higher threshold voltage with aging time is consistent with that observed in the B-V analysis. Second, notice that the aging process gradually

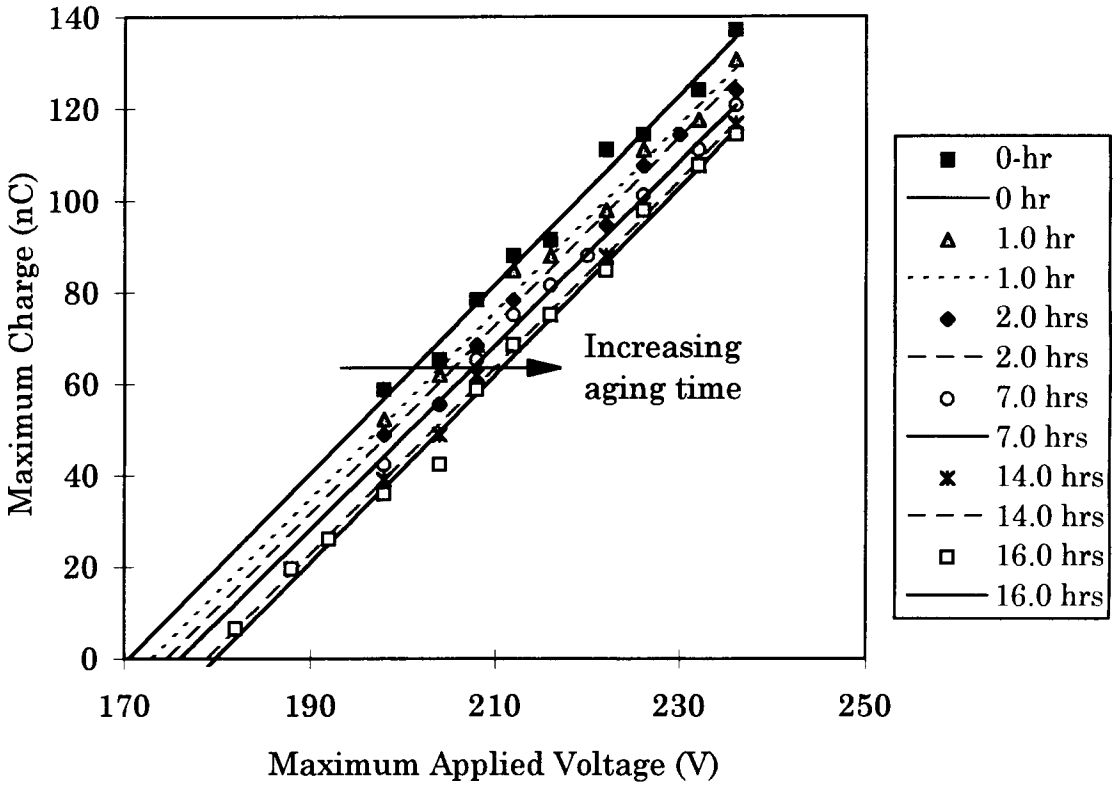

Figure 6.1. Q_{max}-V_{max} curves corresponding to various aging times.

becomes more stable with aging time. It is commonly seen that the threshold voltage of thiogallate TFEL devices increases dramatically, between 10 to 12

V, during the first 15 minutes of operation. After that, the device still ages with operating time, but only slowly, and eventually becomes more stable.

Figure 6.2 shows Q-F_p curves corresponding to various aging times. It is evident from Fig. 6.2 that there is a reduction of conduction charge, due to a reduction of electron emission from the interface, as seen by the gradual decreasing slope of the BC and GH regimes. The decreasing slope in the BC and GH regimes of the Q-F_p curves with aging time is consistent with a reduction of C_{eff} in C-V curves, see Fig. 6.3

In summary, the experimentally established aging trends are that with increasing aging time: the threshold shifts to higher voltages (i.e. a p-

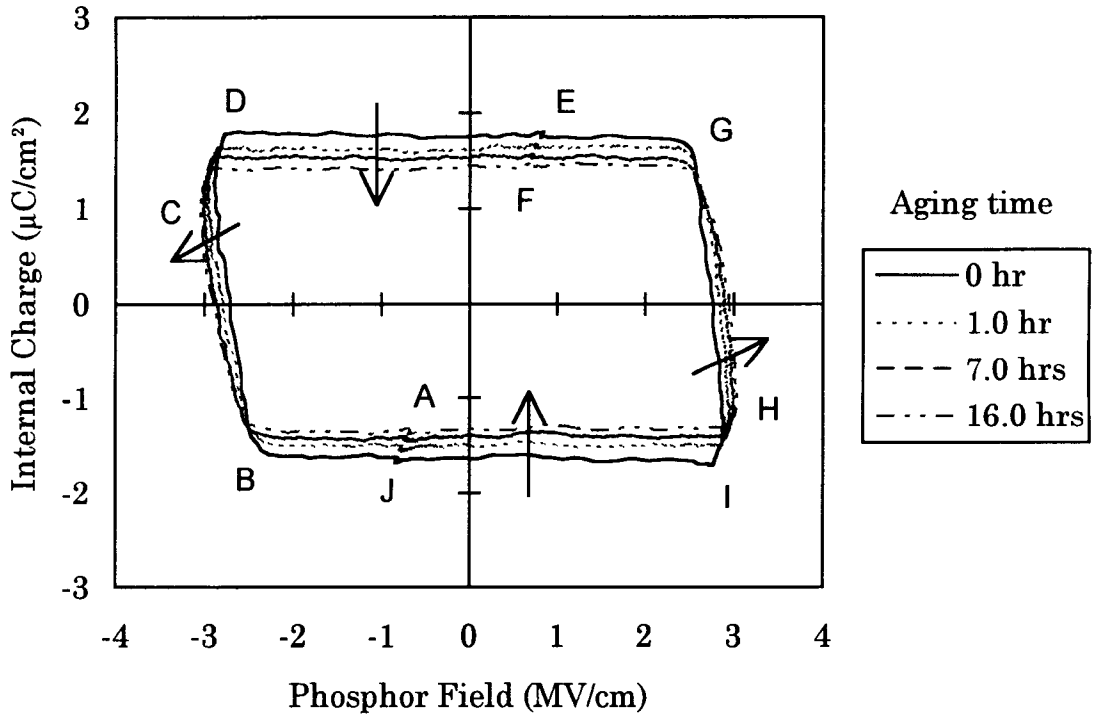

Figure 6.2. Q-F_p curves corresponding to various aging times.

shift), the Q_{max}-V_{max} and C-V curves shift rigidly to higher voltages, the conduction charge decreases, the slope of the BC and GH portions of the Q-F_p curves decreases, and C_{eff} decreases. These aging trends are very similar to trends observed by Davidson *et. al.* [13] in their aging study of evaporated ZnS:Mn TFEL devices, except that C_{eff} was constant and equal to the physical insulator capacitance for their devices. This difference is due to the

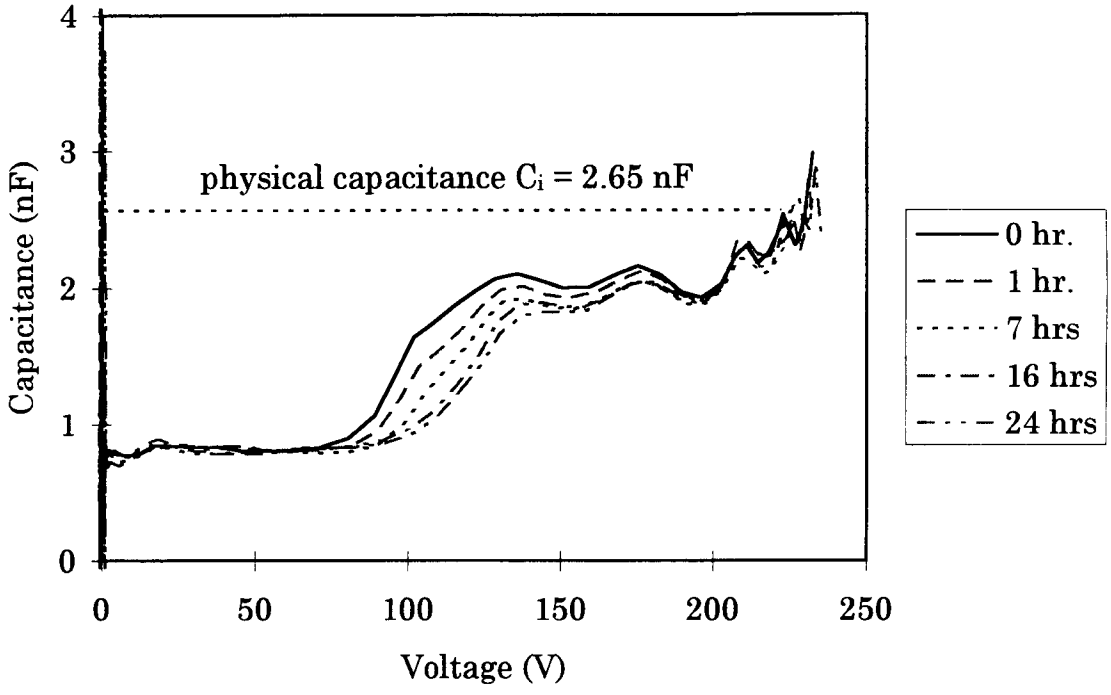

Figure 6.3. C-V curves corresponding to various aging times.

fact that Davidson *et. al.*'s devices exhibit field-clamping (i.e. M = 1) whereas the thiogallate devices used in the present study show M < 1 behavior, in

which there is an inadequate amount of conduction current for field-clamping to occur. Even though the C_{eff} aging is believed to be very similar for evaporated ZnS:Mn and thiogallate TFEL devices since these C_{eff} differences only relate to whether or not field clamping occur. Thus, the same model proposed by Dadvison *et. al.* is invoked to account for aging trends in thiogallate TFEL devices. This aging model involves the creation of deep level, fixed charge trap states due to atomic inter-diffusion at the

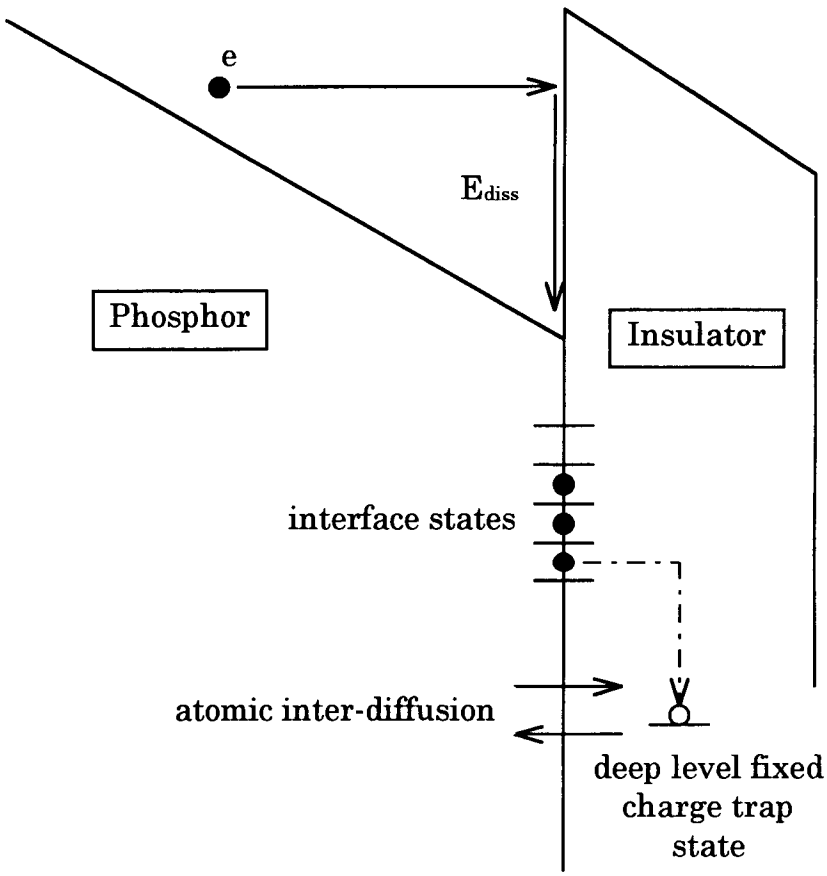

Figure 6.4. Proposed aging mechanism for thiogallate TFEL devices.

phosphor/insulator interface. The atomic inter-diffusion is believed to be enhanced by the thermalization energy dissipated (E_{diss}) when hot electrons impinge at the phosphor/insulator conduction band discontinuity. This aging mechanism is illustrated in Fig. 6.4. Further discussion of this aging model may be found in reference (14).

6.3 Variable Temperature Experimental Results

These experiments are accomplished by applying a high voltage standard bipolar pulse to the TFEL device, keeping V_{max} (40 V above the threshold voltage) and frequency (60 or 200 Hz) constant, and monitoring the luminance, C-V, Q-V, Q-F_p, and Q_{max}-V_{max} characteristics as a function of temperature. These experiments are performed at a low frequency (i.e. 60 Hz) in order to minimize the effects of self-heating of the device. The temperature control is accomplished using a Sun System model EC1A environmental chamber which provides a temperature range of -185°C to 315°C.

To test the effects of temperature on the thiogallate TFEL device operation, a standard blue thiogallate device is tested under a constant bipolar waveform at various temperature in a range of 30°C to 150°C. The experimental results are plotted in Fig. 6.5. This test is performed at a frequency of 60 Hz. From this plot it is seen that the luminance of the

thiogallate device at 150°C is reduced to approximately 50% of its room temperature value, whereas the conduction charge increases by approximately 10%. Note that there are two different slopes in the luminance curve. This suggests that there are two different quenching mechanisms that contribute to the reduction of luminance of this device in the two different temperature regimes. A decrease of luminance with increasing temperature is called thermal quenching. It is an undesirable feature of a TFEL display device since heat generated by the driver circuitry, which is mounted on the back of the display, may cause a brightness

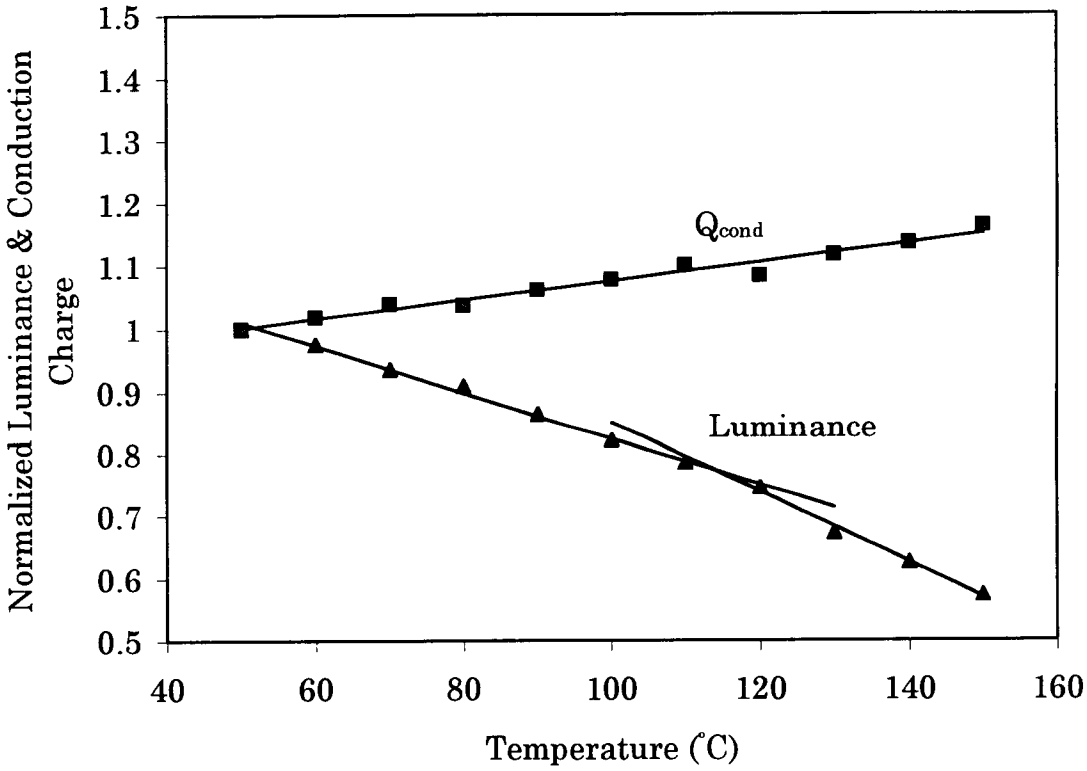

Figure 6.5. Luminance and conduction charge for a thiogallate device as a function of temperature.

reduction.

Figure 6.6 shows Q-F_P curves corresponding to various temperatures. It is evident from Fig. 6.6 that the conduction charge increases with increasing temperature whereas the phosphor field slightly decreases. The decrease in the phosphor field is attributed to the fact that the conduction

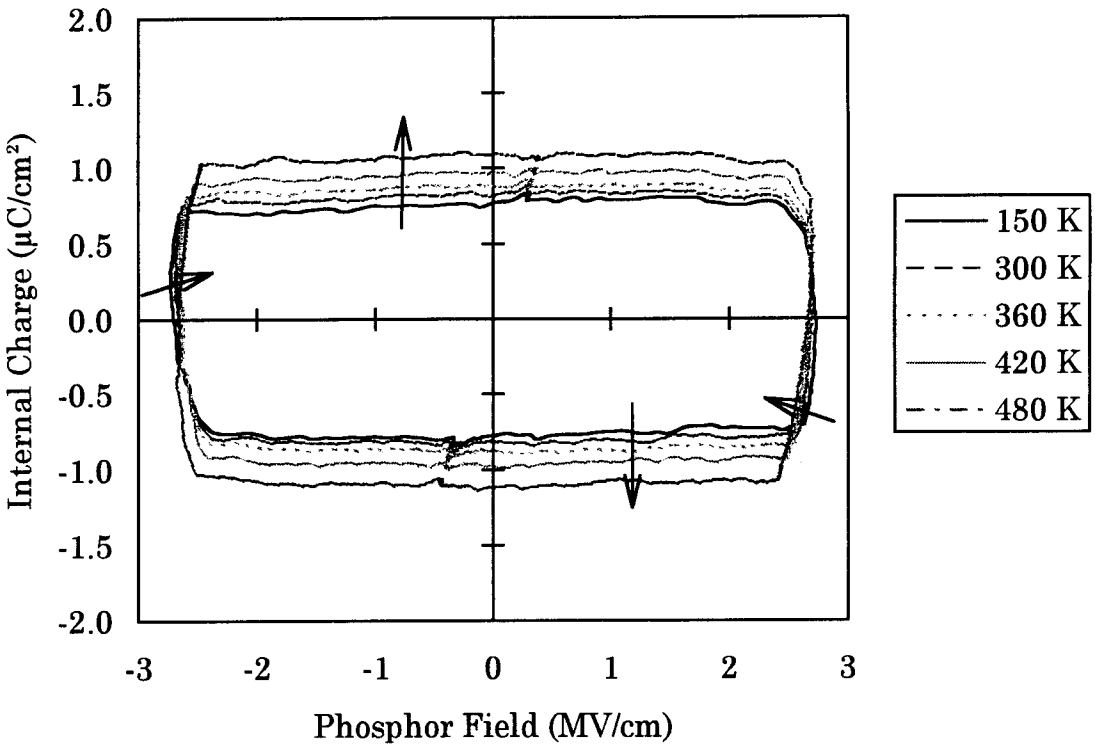

Figure 6.6. Q-F_P curves corresponding to various temperatures. Arrows point in the direction of increasing temperature.

charge increases with increasing temperature due to the increase of electron emission from the interface, as seen by the increase of M with increasing

temperature. This result implies that at least a portion of the electron emission is via phonon-assisted tunneling, in which the emission rate increases with increasing temperature, and not exclusively via pure tunneling, which is temperature-independent. The test shown in Fig. 6.5 is accomplished at temperatures less than 490 K in order to avoid the second thermal quenching regime observed Fig. 6.5. At temperatures higher than 490 K, Q-F_p curves for this TFEL thiogallate device exhibit strange effects which cause a shift in the Q-F_p curves away from the origin, as shown in Fig. 6.7. Q-F_p curves shown in Fig. 6.6 are for a different thiogallate device which

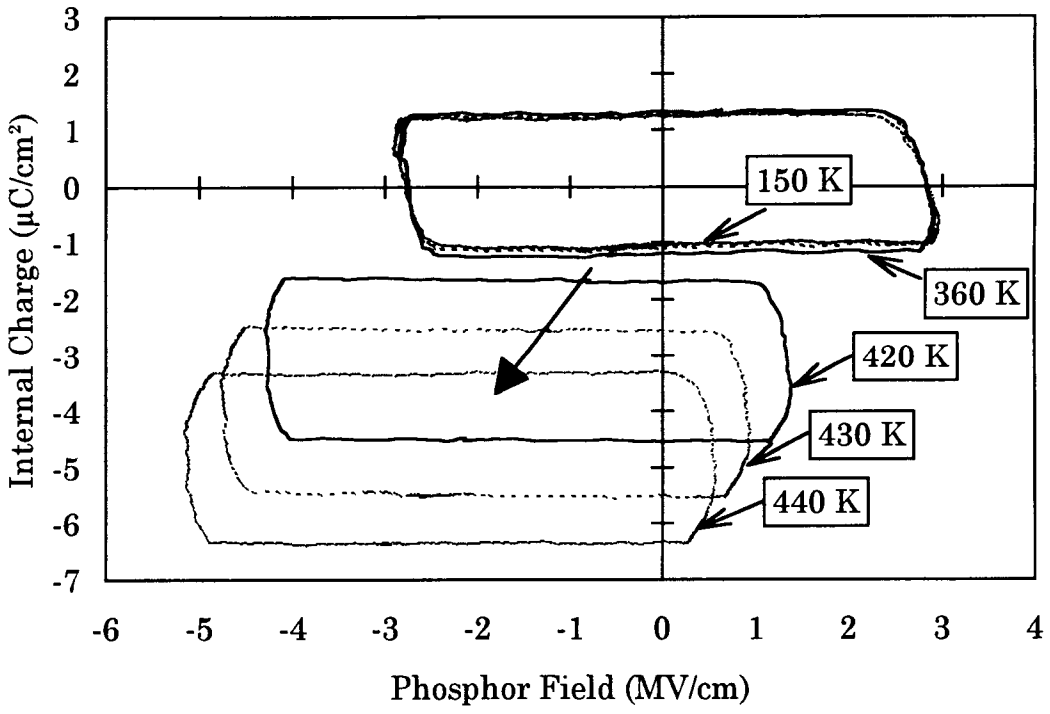

Figure 6.7. Q-F_p curves corresponding to various temperatures.

shows a shift of the Q-F_p curve at temperatures above ~360 K. The shift of the Q-F_p curve is concomitant with the initiation of the second quenching regime observed in Fig. 6.5. Note that the conduction charge continues to increase with increasing temperature for the curves shifted away from the origin.

Figures 6.8 and 6.9 show C-V and Q-V obtained at various temperatures. It is evident from these figures that both C_t and C_{eff} are a function of temperature and that the increase in C_t is small compared to that of C_{eff}. Note that C_{eff} is greater than the physical insulator capacitance at

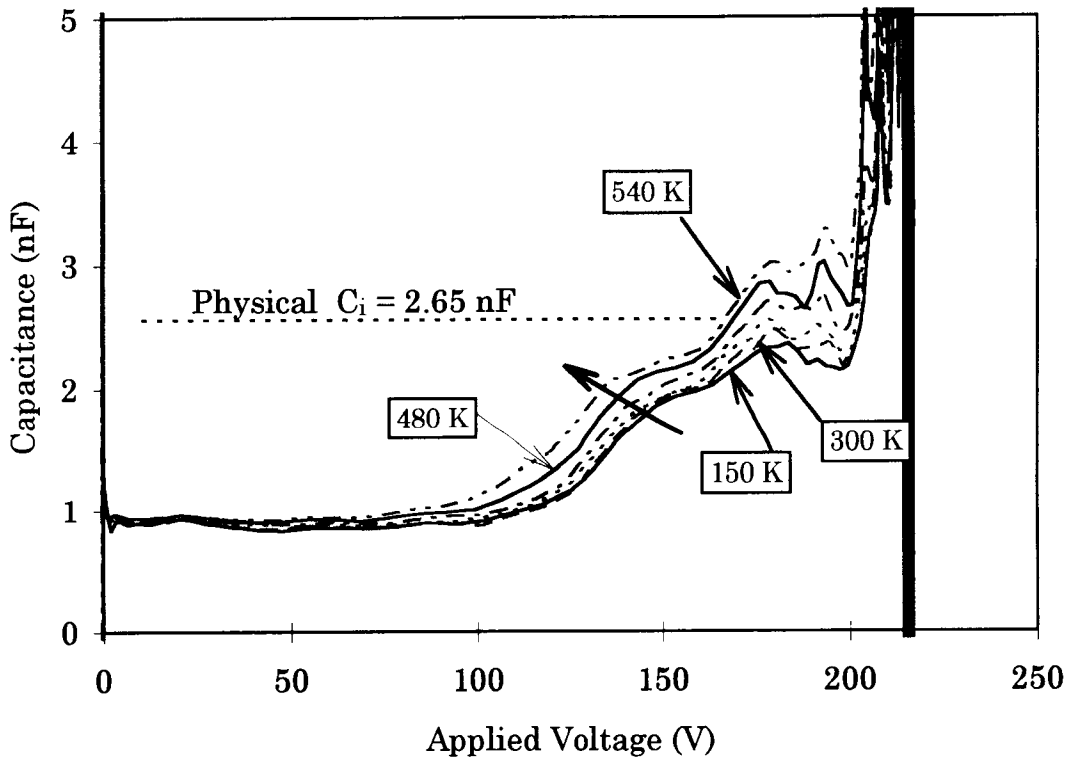

Figure 6.8. C-V curves corresponding to various temperature.

temperatures greater than ~400 K. The fact that C_{eff} is greater than the physical insulator capacitance suggests that charge multiplication exists in the phosphor and that it is more pronounced at high temperature. Furthermore, the C-V curves shift rigidly to lower turn-on voltage with increasing temperature. The rigid-shift to lower voltages of the C-V curve is consistent with charge injection from interface states and the increase in the conduction charge, as seen in Figs. 6.6 and 6.9, which also gives rise to an increase in polarization charge. The shift of Q-F_p curves, observed in Fig. 6.7, and associated with the second thermal quenching regime, shown in

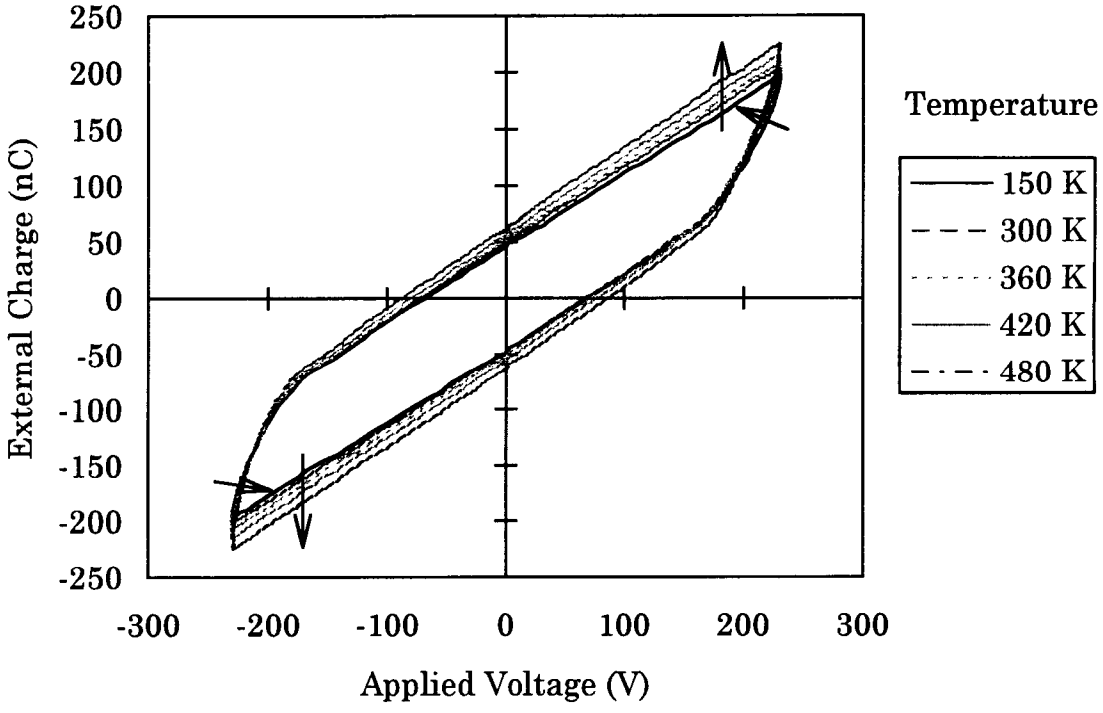

Figure 6.9. Q-V curves corresponding to various temperatures.

Fig. 6.5, is also observed in Q-V curves, as shown in Fig. 6.10. Currently, it is unclear what causes the shift in both Q-V and Q-F_p curves. Preliminary simulations using a single sheet of charge model indicate that it is due to asymmetric generation of space charge in the phosphor layer. [27] Further device simulation work is necessary to explain this behavior in detail.

Figure 6.11 shows Q_{max}-V_{max} curves obtained at various temperatures. It is evident that the threshold shifts to lower voltages with increasing temperature. This is consistent with an increase in polarization charge with

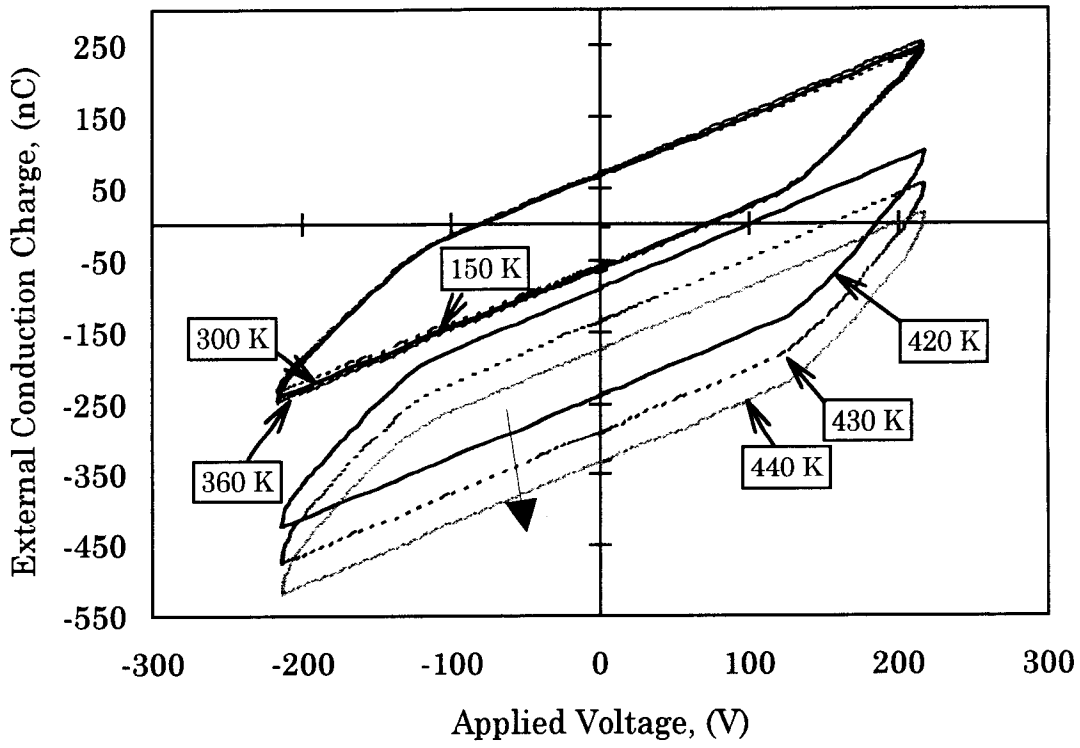

Figure 6.10. Q-V curves corresponding to various temperatures.

increasing temperature. Additionally, the slope of the Q_{max}-V_{max} curves increases with increasing temperature. This is consistent with the increase in conduction charge with increasing temperature.

Experimentally determined electrical trends (i.e. reduction of phosphor field, increase of conduction charge, reduction of threshold voltage, and a rigid-shift of C-V curves with increasing temperature) imply that the increase in the phosphor conduction charge with increasing temperature is due to phonon-assisted tunneling. Thus, the experimental results indicate that phonon- assisted tunneling has a significant role in thiogallate TFEL

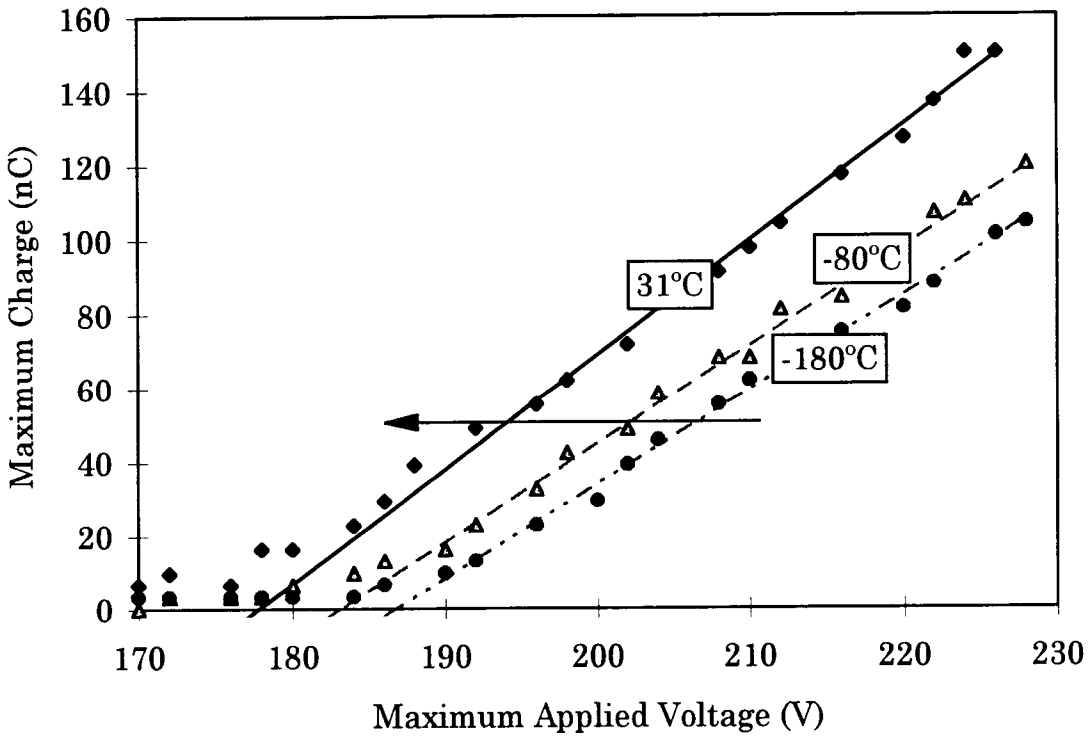

Figure 6.11. Q_{max}-V_{max} curves corresponding to various temperatures.

device operation in terms of electron emission at the phosphor/insulator interfaces. Due to phonon-assisted tunneling contributions, lower electric fields and threshold voltages are required to inject deeply trapped electrons into the phosphor conduction band at higher temperatures. This, in turn, gives rise to an increase of conduction charge at higher temperature.

As a check to the validity of phonon-assisted tunneling as a contributing mechanism for electron emission from interface states, a theoretical plot of the emission rate of thermal-assisted tunneling is compared to that of pure tunneling, using the following equations. The emission rate for phonon-assisted tunneling, $e_n(PAT)$, is given by [15]

$$e_n(PAT) = e_n(TE)\int \exp\left[z - z^{3/2}\left(\frac{8\pi(m^*)^{3/2}}{3qhF_p}\right)\left(1 - \left(\frac{\left[\frac{qF_p}{\pi\varepsilon_p}\right]^{1/2}}{zkT}\right)^{5/3}\right)\right] dz, \quad (6.1)$$

where $e_n(TE)$ is the thermal emission rate given by

$$e_n(TE) = \sigma v_{th} N_c \exp\left(-\frac{E_{qf} - \left[\frac{qF_p}{\pi\varepsilon_p}\right]^{1/2}}{kT}\right) \quad (6.2)$$

and where

k: Boltzman's constant,

T: temperature in Kelvin,

σ: capture cross section,

N_c: effective density of states,

v_{th}: thermal velocity,

h: Plank's constant,

m*: effective mass of electron,

F_p: phosphor field,

E_{qf}: trap depth,

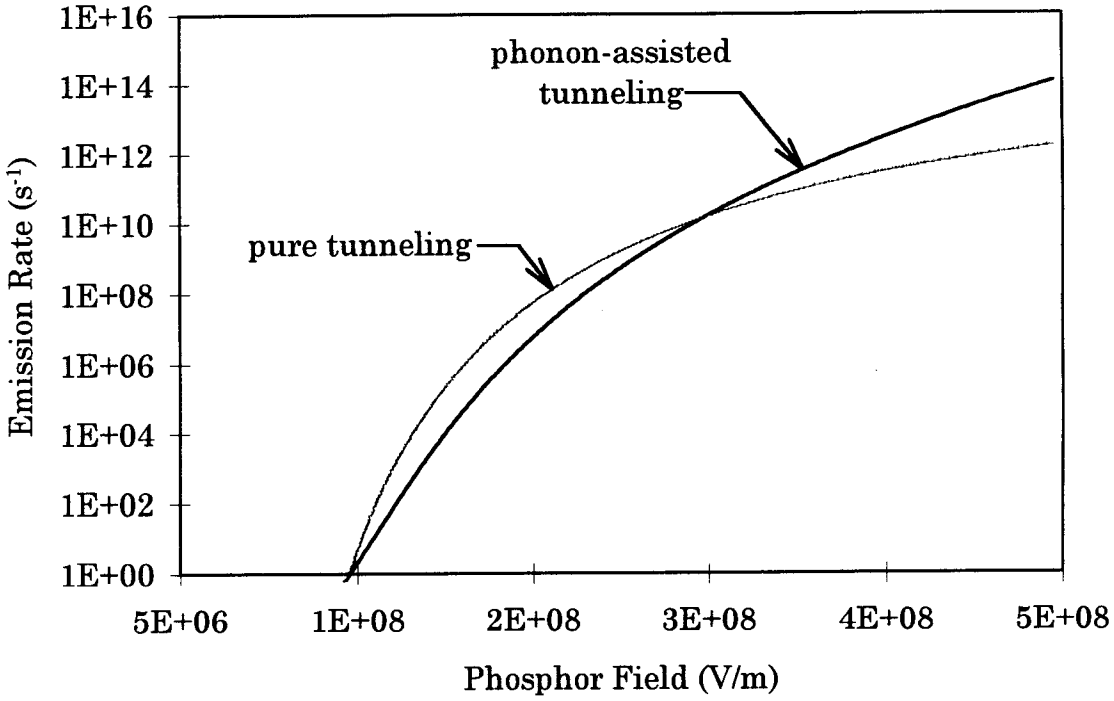

Figure 6.12. Emission rate for pure tunneling and phonon-assisted tunneling versus phosphor field for a ZnS:Mn device.

and z is the normalized energy, which is given by

$$z = \frac{E_{qf}}{kT}. \tag{6.3}$$

The emission rate for pure tunneling, $e_n(PT)$, is given by

$$e_n(PT) = \frac{qF_p}{4\left(2m^* E_{qf}\right)^{1/2}} \exp\left[\left(-\frac{8\pi(2m^*)^{1/2} E_{qf}^{3/2}}{3qhF_p}\right)\left(1-\left(\frac{\left[\frac{qF_p}{\pi\varepsilon_p}\right]^{1/2}}{E_{qf}}\right)^{5/3}\right)\right] \tag{6.4}$$

Using ZnS:Mn TFEL parameters (N_c = 4.12E18 cm^{-3}, E_{qf} = 0.95eV, σ = 10E-20 cm^3) [15] a plot of $e_n(PAT)$ and $e_n(PT)$ versus phosphor field at room temperature is show in Fig. 6.12.

Figure 6.12 shows that for a typical range of phosphor fields (2.5 - 3.5 MV/m) for thiogallate TFEL device operation, the emission rate for phonon-assisted tunneling is comparable to that for pure tunneling for ZnS:Mn TFEL devices. The appropriate model parameters (i.e. N_c, E_{qf}, and σ) for thiogallate devices are unknown. However, from Chapter 4, it is found that the interface states of thiogallate devices are deeper in energy than that of ZnS:Mn devices. Thus, if it is assumed that E_{qf} = 1.1 eV and σ = 1E19 cm^3, Fig. 6.13 results. Once again, this simulation shows that the emission rate for phonon-assisted tunneling is comparable to that of pure tunneling. Therefore, from the experimental results and from Figs. 6.13 and 6.13, it appears likely that phonon-assisted tunneling also has a significant role in

the operation of the thiogallate TFEL devices studied herein.

The thermal quenching observed in Fig. 6.5 may be attributed to one of the following mechanisms: (1) a reduction of the phosphor field; (2) phosphor

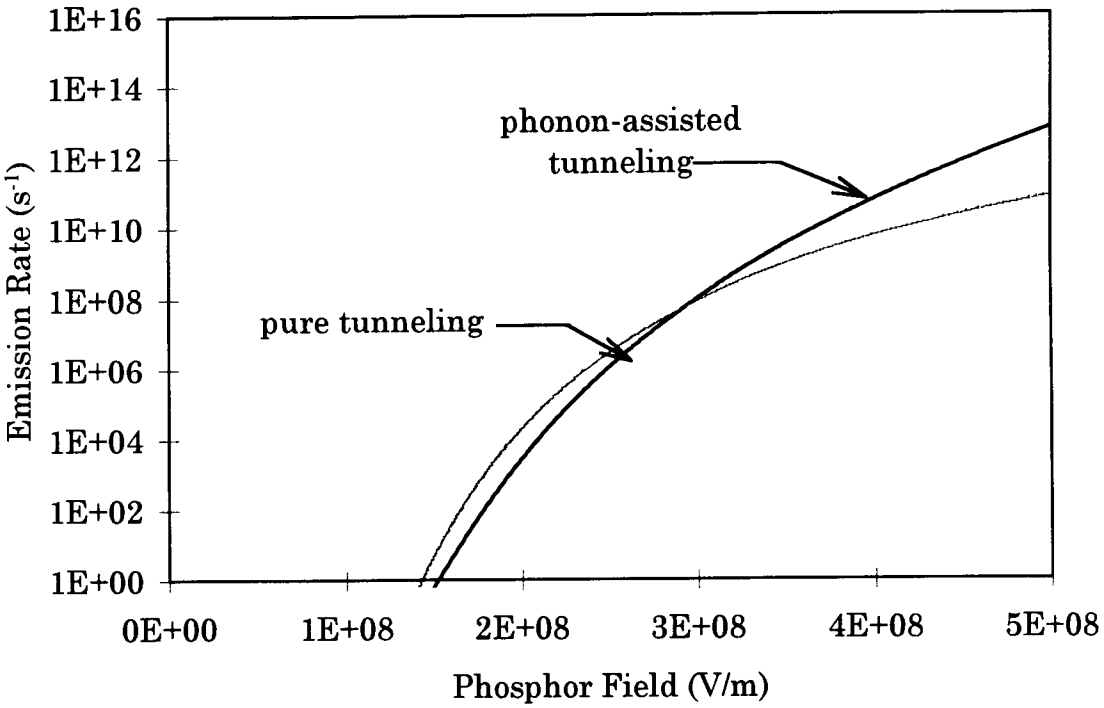

Figure 6.13. Emission rate for pure tunneling and phonon-assisted tunneling versus phosphor field for a device with E_{qf} = 1.1 eV and σ = 1E19 cm^3.

and insulator dielectric constants that are a function of temperature; (3) Ce ionization; (4) a decrease in the de-excitation efficiency due to non-radiative de-excitation of Ce; (5) a decrease in the electron transport efficiency or excitation efficiency due to an increase in phonon scattering and a concomitant cooling of the hot electron distribution. These possible

mechanisms are considered individually, as follows.

The reduction of the phosphor field shown in Fig. 6.6 is too small to account for a 50% reduction of the luminance observed in Fig. 6.5; therefore it is very unlikely that the phosphor field reduction is the main source of thermal quenching. This assertion is supported by the following analysis. A relation for the luminance in terms of the phosphor threshold field is given by [10]

$$L = \frac{4}{\pi}\eta f \varepsilon_o \varepsilon_I \left(\frac{d_p}{d_I}\right) F_{p,th}(V_a - V_{th}) \qquad (6.5)$$

where $(V_a\text{-}V_{th})$ is the modulation voltage, η is the experimental luminous efficiency which is associated with the excitation and de-excitation efficiency, f is the waveform frequency, ε_I is the insulator dielectric constant, $F_{p,th}$ is the phosphor threshold field, V_a is the applied voltage, and d_p and d_I are the phosphor and insulator thicknesses, respectively. From Eq. 6.5, one can see that a small reduction of the phosphor field observed in Fig. 6.6 is not enough to account for a 50% decrease in the luminance exhibited in Fig. 6.5. Therefore, the phosphor field reduction is unlikely to be the main reason for the thermal quenching.

The effects of the phosphor dielectric constant on the luminance can be seen using a simple 2-capacitor equivalent circuit model, as shown in Fig. 6.14, where C_I is a lumped capacitor consisting of the insulator capacitances and C_p is a phosphor capacitor. The amount of voltage dropped across the

phosphor layer for a given applied voltage V_a is given by

$$V_P = \frac{C_I}{C_I + C_P} V_a \tag{6.6}$$

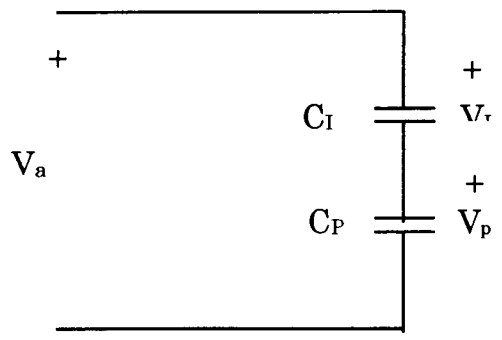

Figure 6.14. A simple 2-capacitor circuit model for a TFEL device.

and the phosphor field at threshold voltage is given by

$$F_{P,th} = \frac{1}{d_P} \frac{C_I}{C_I + C_P} V_{th} \tag{6.7}$$

or

$$F_{P,th} = \frac{1}{d_P} \frac{\varepsilon_I}{\varepsilon_I + \varepsilon_P \left(\frac{dI}{dp} \right)} V_{th} \ . \tag{6.8}$$

Recall that for an ideal TFEL device, the clamping or turn-on field in the phosphor is basically equal to its threshold field. Substitute Eq. 6.8 into 6.5 to obtain

$$L = \frac{4}{\pi} \eta f \varepsilon_0 \varepsilon_I \left(\frac{1}{d_P} \right) \frac{\varepsilon_I}{\varepsilon_I + \varepsilon_P \left(\frac{d_I}{d_d} \right)} V_{th} (V_a - V_{th}) . \tag{6.9}$$

Equation 6.9 clearly indicates that a small increase in the phosphor dielectric constant, as shown in Figs. 6.8 and 6.9, is not enough to justify a large reduction of the luminance, as observed in Fig. 6.5.

Therefore, the thermal quenching trends observed in Fig. 6.5 are likely due to one or a combination of the effects associated with a decrease in the de-excitation efficiency, electron transport efficiency, or Ce ionization at high temperature. It is still unclear which mechanism dominates in the thermal quenching of TFEL thiogallate devices. However, the luminescent characteristics observed in Fig. 6.5 suggest that there are two distinct

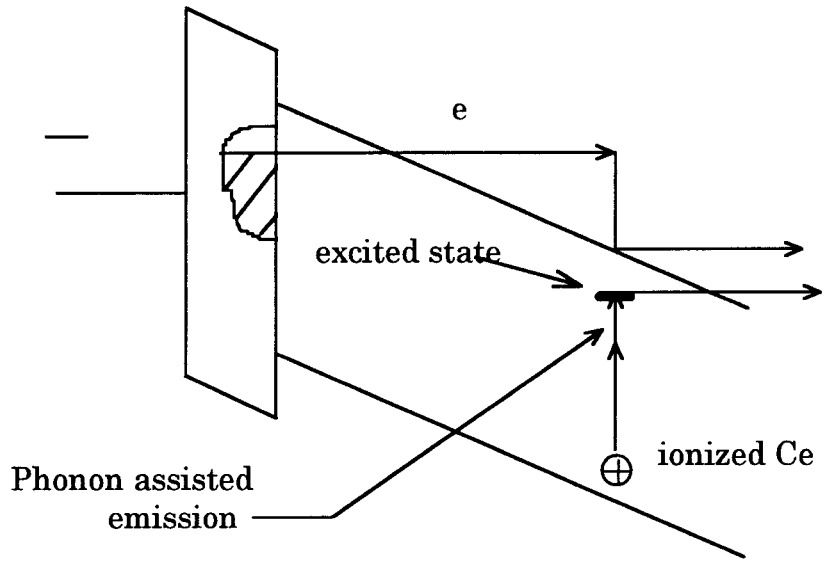

Figure 6.15. Ionized Ce due to phonon-assisted tunneling.

mechanisms that contribute to the reduction of luminance: one at low temperatures and the other at more elevated temperatures. The first region of the thermal quenching curve is attributed to a decrease in the de-excitation and/or electron transport efficiency. At more elevated temperatures, thermal quenching is caused by an additional mechanism, probably the ionization of Ce via phonon-assisted tunneling in which excited Ce atoms are ionized to the conduction band, as shown in Fig. 6.15. Attributing the elevated temperature thermal quenching regime to Ce ionization is appealing since Q-F_p and Q-V shifting occurs in this quenching regime and this shifting is attributed to the asymmetrical generation of phosphor space charge.

Chapter 7 - Conclusions and Recommendations for Future Work

7.1 Conclusions

The primary contributions of this thesis are the electrical characterization of thiogallate TFEL devices and a comparison to the electrical characteristics of evaporated ZnS:Mn TFEL devices, experimental evidence for positive and negative space charge in the thiogallate phosphor, and the aging and temperature studies of thiogallate TFEL devices. Additionally, a direct way to obtain Q_{max}-V_{max} curve from a measurement of $q_{ext}(t)$ curves as a function of V_{max}, is developed.

Comparison of the electrical characteristics of thiogallate to that of evaporated ZnS:Mn TFEL devices through the use of C-V, Q-F_p, and Q_{max}-V_{max} analysis techniques shows that the blue-emitting thiogallate devices exhibit no field-clamping or band-to-band impact ionization. Interface states of thiogallate devices are deeper in energy than that of ZnS:Mn devices, which results in very small leakage charge for thiogallate devices.

Evidence is presented for the existence of both positive and negative space charge in the phosphor and that the nature or absence of this space charge depends on the nature of the device fabrication process employed. An indium-injection layer in the thiogallate device results in the existence of negative space charge in the phosphor which subsequently results in an increase of the turn-on field with increasing V_{max}. Experimental results also

indicates that incorporation of an injection layer can be used in the improvement of the TFEL device in terms of increasing the luminance and lowering the threshold voltage.

Aging and temperature studies are performed to investigate the stability of the thiogallate device and to establish aging mechanisms. Aging studies show that the aging mechanism of thiogallate devices is similar to that of the ZnS:Mn TFEL devices. Aging trends reveal that the increase in the threshold voltage and the decrease in the conduction charge with increasing aging times is mainly due to the creation of deep level, fixed charge traps at the interface. Variable temperature studies show that thiogallate devices exhibit thermal quenching. A plot of the luminescence versus temperature indicates that there are at least two mechanisms that contribute to thermal quenching in thiogallate devices; one at low temperatures and the other at higher temperatures. Low temperature thermal quenching is attributed a decrease of the de-excitation efficiency and/or the electron transport efficiency, whereas high temperature quenching is ascribed to Ce ionization which causes a steeper drop in luminance at high temperatures. Variable temperature studies indicate that phonon-assisted tunneling has a significant role in the device operation of thiogallate TFEL devices.

7.2 Recommendations for Future Work

Knowledge of the interface state density and distribution is necessary in order to obtain a more complete understanding of the device physics of thiogallate and other TFEL devices.

Experimental results presented herein indicate that thermal quenching is an important issue in determining the stability of thiogallate TFEL device operation. This is especially true due to the structure of the EL flat panel display since heat is generated from the driver circuitry. Therefore, further temperature studies are necessary to determine which mechanism (de-excitation efficiency, transport efficiency, or Ce ionization) dominates the thermal quenching of thiogallate device. Due to the extremely short decay time of Ce, nanosecond resolution, optical measurements are needed in order to determine the de-excitation efficiency of thiogallate device.

Long-term aging studies are necessary. Aging studies should be conducted at different temperatures to determine the long-term stability of these TFEL device and further establish in detail the aging mechanisms.

BIBLIOGRAPHY

1. W.A. Barrow, R.E. Coovert, and C.N. King, "Strontium Sulphide: The Host for a New High Efficiency Thin Film EL Blue Phosphor," Digest of the 1984 SID Intt'l display Symposim, p. 249, 1984.

2. T.E. Peters and J.A. Baglio, "Luminescence and Structural Properties of Thiogallate Phosphor Ce and Eu - Activated Phosphors. Part I," J. Elec. soc. 119, p. 230, 1970.

3. W.A. Barrow, R.C. Coovert, E. Dickey, C.N. King, C. Laakso, S.S. Sun, R.T. Tuenge, R. Wentross, and J. Kane, "A New Class of Blue TFEL Phosphors with Applications to a VGA Full Color Display," Digest of 1993 SID Int'l Display Symposium, p. 761, 1993.

4. L.V. Pham, J.F. Wager, S.S. Sun, E. Dickey, R.T. Tuenge, and C.N. King, "Electrical Characterization of Blue Electroluminescent Devices,"in Advanced Flat Panel Display Technology, edited by P.S. Friedman, SPIE Proceedings 2174, p. 190, 1994.

5. G. Destriau, "Recherches sur les Scintillations des Zinc aux Rayons", Journal de Chime Physique, 33, p. 587, 1936.

6. N.A. Vlasenko and Iu. A. Poplov, "Study of the Electroluminescence of a sublimed ZnS-Mn Phosphor", Optics and Spectroscopy 8, p. 39, 1960.

7. M.J.Russ and D.I. Kennedy, "The Effects of Double Insulating Layers on the Electroluminescence of Evaporated Zns:Mn Films,"J. Electrochem. Soc., 114, p.1066, 1967.

8. T. Inoguchi, M. Takeda, Y. Kakihora, and M. Yoshida, "Stable High Luminance Thin-Film Electroluminescent Panels,"Digest 1974 SID Int'l Symp., p. 86, 1974.

9. M. Takeda, Y. Kanatani, H. Kishishita, and H. Uede, Proc. SPIE 386, Advances in Display Technology III, p. 34, 1983.

10. Y.A. Ono, "Electroluminescent display," World Scientific Publishing Co. Pte. Ltd. 1995.

11. R.T. Tuenge and J. Kane, "Bright Red EL Using a Thin-Film Filter," Digest of 1991 SID Int'l Symposium, p. 279, 1991.

12. H. Ohnishi, K. Yamamoto and Y. Katayama, "Improved Efficiency of Green-Color ACTFEL Devices Grown by rf-Sputtering," Conf. Record of the 1985 Int'l Display Rsch. Cong., p. 159, 1985.

13. G. Häkönen, K. Härkönen, R. Törnqvist, "Green Emitting Thin-Film Electroluminescent Device Grown by Atomic Layer Epitaxy," Digest of 1990 SID Int'l Symposium, p. 232, 1991.

14. J.D. Davidson, M.S. Thesis, Oregon State University, 1991.

15. A.A. Douglas, M.S. Thesis, Oregon State University, 1993.

16. P.M. Alt, "Thin-Film EL Devices: Device Characteristics and Performance," Proc. of the SID, 25, no. 2, p. 123, 1984.

17. D.H. Smith, "Modeling a.c. Thin-Film Electroluminescent Devices," J. Lum., vol. 23, P. 209, 1981.

18. J.D. Davidson, J.F. Wager, I. Khormaei, C.N. King, R. Williams, "Electrical Characterization and Modeling of Alternating-Current Thin-Film Electroluminescent Devices," IEEE Trans. on Elect. Dev., vol. 39, no. 5, p. 1122, 1992.

19. A.A. Douglas and J.F. Wager, "Electrical Characterization and Modeling of ZnS:Mn ACTFEL Devices with Various Pulse Waveforms," Digest 1992 SID Int'l Symposium, p. 356, 1992.

20. R.C. McArthur, J.D. Davidson, J.F. Wager, I. Khormaei, and C.N. King "Capacitance-Voltage Characteristics of Alternating-Current Thing-Film Electroluminescent Devices," Appl. Phys. Lett., vol. 56, p. 1889, 1990.

21. A. Abu-Dayah, J.F. Wager, and S Kobayashi, "Internal Charge-Phosphor Field Characteristics of Alternating-Current TFEL Devices", Appl. Phys. Lett. 62, 744, 1993.

22. J.F. Wager, A.A. Douglas, and D.C. Morton, "Electrical Characterization and modeling of ACTFEL devices", Electroluminescence, p. 92, 1992.

23. W.M. Ang, S. Pennathur, L. Pham, J.F. Wager, and S.M. Goodnick, "Evidence for Band-to-Band Impact Ionization in Evaporated ZnS:Mn Alternating-Current Thin-Film Electroluminescent Devices," J. Appl. Phys. 77, 1995.

24. E. Bringuier, J. Appl. Phys. "Electron multiplication in ZnS-type electroluminescent devices", 67, 7040, 1990.

25. E. Briguier, "Charge Transfer in ZnS-Type Electroluminescence," J. Appl. Phys, vol. 66, no. 3, p. 1314, 1989.

26. A. Abu-Dayah, M.S. Thesis, Oregon State University, 1993.

27. P.D. Keir (private communication).